

1                   **Physics-guided deep learning model for daily**  
2                   **groundwater table maps estimation using passive**  
3                   **surface-wave dispersion**

4                   **José Cunha Teixeira <sup>1,2</sup>, Ludovic Bodet <sup>1</sup>, Agnès Rivière <sup>3</sup>, Amélie Hallier <sup>2</sup>,**  
5                   **Alexandrine Gesret <sup>3</sup>, Marine Dangeard <sup>2</sup>, Amine Dhemaied <sup>2</sup>, Joséphine**  
6                   **Boisson Gaboriau <sup>2</sup>,**

7                   <sup>1</sup>Sorbonne Université, CNRS, EPHE, UMR 7619 METIS, 4 place Jussieu, 75252 Paris 05, France

8                   <sup>2</sup>SNCF Réseau, 6 avenue François Mitterrand, 93210 Saint-Denis, France

9                   <sup>3</sup>Geosciences Department, Mines Paris - PSL, PSL University, Paris, France

10                   **Key Points:**

- 11                   • Estimating ground water table (GWT) maps from seismic dispersion with deep learn-  
12                   ing.
- 13                   • Understanding the spatial and temporal dynamic of the GWT with high resolution.
- 14                   • Using the GWT geometry and dynamic to constrain the geologic model of the site.

---

Corresponding author: José Cunha Teixeira, [jose.teixeira@sorbonne-universite.fr](mailto:jose.teixeira@sorbonne-universite.fr)

**Abstract**

Monitoring groundwater tables (GWTs) is challenging due to limited spatial and temporal observations. This study presents an innovative approach utilizing supervised deep learning, specifically a Multilayer Perceptron (MLP), and continuous passive-Multichannel Analysis of Surface Waves (passive-MASW) for constructing 2D GWT level maps. The study site, geologically well-constrained, features two 20-meter-deep piezometers and a permanent 2D geophone array capturing train-induced surface waves. For each point of the 2D array, dispersion curves (DCs), displaying Rayleigh-wave phase velocities ( $V_R$ ) across a frequency range of 5 to 50 Hz, have been computed each day between December 2022 and September 2023. In the present study, these DCs are resampled in wavelengths ranging from 4 to 15 m in order to focus the monitoring on the expected GWT levels (between -1 and -5 m). Nine months of daily  $V_R$  data around one of the two piezometers is used to train the MLP model. GWT levels are then estimated across the entire geophone array, generating daily 2D GWT maps. Model's performance is tested through cross-validation and comparisons with GWT level data at the second piezometer. Model's efficiency is quantified with the root-mean-square error (RMSE) and the coefficient of determination ( $R^2$ ). The  $R^2$  is estimated at 80% for data surrounding the training piezometer, and at 68% for data surrounding the test piezometer. Additionally, the RMSE is impressively low at 0.03 m at both piezometers. Results showcase the effectiveness of DL in estimating GWT level maps from passive-MASW data, offering a practical and efficient monitoring solution across broader spatial extents.

**Plain Language Summary**

This study introduces an innovative method for monitoring groundwater table levels, using a combination of deep learning and passive surface-wave data. The study site, features two piezometers, and a sensor array capturing seismic waves induced by passing trains providing daily seismic wave velocity data, from December 2022 to September 2023. A Multilayer Perceptron model was trained using groundwater table level data from one piezometer and seismic data at the same location. Subsequently, the trained model was applied to estimate groundwater table levels across the entire sensor array area, generating daily maps. The accuracy of the model was tested, revealing an 80% accuracy around the piezometer used in training, and 68% for the other piezometer. Notably, the estimation errors were remarkably low. This research demonstrates the effective use of deep learning in estimating groundwater table levels from passive surface-wave data. It contributes

47 to the understanding of underground water dynamics, offering a valuable tool for water  
48 resource management and environmental hazard monitoring. Importantly, this method al-  
49 lows for efficient groundwater monitoring across large areas using limited data from a single  
50 piezometer.

## 51 **1 Introduction**

52 Groundwater (GW) systems are in dynamic balance between climatic forcing and hu-  
53 man pressure. They play a pivotal role in addressing various water resource management  
54 and civil engineering matters. Monitoring the dynamics of groundwater table (GWT) ge-  
55 ometry is essential for evaluating the resilience and quality of aquifers, predicting water  
56 availability, and allowing for sustainable extraction and use, particularly during extreme  
57 floods and droughts. Additionally, this understanding proves equally crucial for identifying  
58 high-risk infrastructures susceptible to GW-induced natural hazards. In fact, GW floods,  
59 landslides (Rahardjo et al., 2010; Panda et al., 2022), and sinkholes (Waltham et al., 2004;  
60 Gutiérrez et al., 2014; Parise, 2019; Xiao et al., 2020) are potential threats that can be  
61 anticipated and mitigated more effectively by incorporating knowledge of GWT dynamics.

62 GWTs evolve beneath our feet and still represent a *terra incognita* (Kleinmans, 2005).  
63 The assessment of their geometry and dynamics remains a scientific barrier to be lifted.  
64 While piezometers can punctually measure GWT levels with high precision and accuracy,  
65 it is important to acknowledge that their deployment is often spatially limited, resulting  
66 in sparse estimations across larger areas. To reduce this limitation, GWT maps are of-  
67 ten interpolated from piezometric data, through techniques such as linear estimators and  
68 kriging (Maillot et al., 2019), and represent an important tool for hydrogeologists and civil  
69 engineers. While interpolation techniques offer unbiased results for GWT geometry, they  
70 do not account for the soil spatial heterogeneity between piezometers and are limited by  
71 the spatial distribution and number of piezometers. The effectiveness of the interpolation is  
72 contingent on the availability and strategic placement of these monitoring points, impacting  
73 the overall accuracy and reliability of the generated GWT maps.

74 One effective solution to address this limitation involves the conversion of lithofacies  
75 into hydrofacies information to constrain GWT map interpolations and simulations (Dagan,  
76 1982; Tsai & Li, 2008). The integration of geophysical data can significantly enhance hydro-  
77 logical knowledge by providing spatial information where conventional hydrological measure-

78 ment techniques are limited (Dafflon et al., 2009). Time-lapse geophysical methods, offer  
79 real-time data on changes in subsurface properties, aiding in the characterization of GWT  
80 geometry and the identification of spatial variability and temporal trends (Dangeard et al.,  
81 2021; Hermans et al., 2023). Methods such as ground-penetrating radar (GPR), induced  
82 polarization, self-potential, and resistivity, use the electrical and magnetic properties of the  
83 near-surface and are relevant in assessing soil water content (Garambois et al., 2002; Lo-  
84 effer & Bano, 2004; Samouëlian et al., 2005; Jougnot et al., 2015; Klotzsche et al., 2018).  
85 However, they can be ineffective in very electrically conductive or resistive environments.  
86 Active seismic approaches, such as seismic reflection, refraction and Multichannel Analysis  
87 of Surface Waves (MASW) (Park et al., 1999) have been successfully used for water con-  
88 tent monitoring (Lu, 2014; Bergamo et al., 2016) and 1D GWT geometry characterization  
89 (Pasquet et al., 2015a, 2015b; Dangeard et al., 2021). They mostly rely on the study of  
90 the pressure-(P) and shear-(S) wave velocities ( $V_P$  and  $V_S$ ) to estimate  $V_P/V_S$  or Poisson's  
91 ratios (Biot, 1956a, 1956b), which are sensitive indicators of fluid presence. However they  
92 face limitations due to the difficulty to regularly deploy active sources in adverse conditions,  
93 making continuous characterizations impossible.

94 Passive seismic methods, use continuous and coherent ambient seismic noise generated  
95 by natural or anthropogenic activities. They rely on seismic interferometry and consist in  
96 the Green's function retrieval by cross-correlation between recording sensors pairs to provide  
97 a characterization of the propagation medium (Aki, 1957; Derode et al., 2003; Weaver &  
98 Lobkis, 2004; Wapenaar, 2004; Wapenaar et al., 2010a, 2010b; Larose et al., 2015). Some  
99 approaches monitor the relative temporal variation of seismic velocities ( $dv/v$ ) for specific  
100 wavefronts between pairs of sensors, and have put on evidence a clear correlation with GWT  
101 level variations (Grêt et al., 2006; Voisin et al., 2016; Lecocq et al., 2017; Voisin et al., 2017;  
102 Clements & Denolle, 2018; Garambois et al., 2019; Kim & Lekic, 2019; Barajas et al., 2021;  
103 Mao et al., 2022; Qin et al., 2022; Zhang et al., 2023). Although these methods are able  
104 to generate 2D GWT variation maps, as recently shown by Gaubert-Bastide et al. (2022),  
105 they provide limited information about the aquifer geometry and the proper GWT levels.

106 Another employed approach is the passive-MASW, an extension of the standard active-  
107 MASW. This technique relies on the propagation of ambient Rayleigh-waves, induced by  
108 cars or trains, through linear geophone arrays to characterize the near-surface and has found  
109 application in various civil engineering contexts, both sporadically in time with 1D setups  
110 (Park & Miller, 2008; Quiros et al., 2016; Cheng et al., 2015, 2016; Mi et al., 2022; Czarny

111 et al., 2023; Rezaeifar et al., 2023; You et al., 2023; Mi et al., 2023; Cunha Teixeira et  
112 al., submitted), and for continuous sinkhole monitoring with 2D configurations (Bardaine  
113 & Rondeleux, 2018; Bardainne et al., 2022; Tarnus et al., 2022a, 2022b; Bardainne et al.,  
114 2023). The characterization process is based on the analysis of dispersion curves (DCs),  
115 which depict the fluctuation of Rayleigh-wave phase velocity ( $V_R$ ) across frequencies, along  
116 the linear arrays.  $V_R$  variation over frequency, seen in DCs, is closely linked to the medium's  
117  $V_S$  variation over depth, which, is influenced by the water content (Solazzi et al., 2021). Nev-  
118 ertheless, the shift from dispersion curves (DCs) to ground models incorporating water satu-  
119 ration profiles and GWT level information involves intricate inversion operations, combining  
120 geophysical and hydrogeological data, that are still under development (Sanchez Gonzalez  
121 et al., in prep).

122 Piezometers offer valuable but localized and sparse hydrogeological data, while geo-  
123 physical methods help in interpolating and extrapolating this information. However, geo-  
124 physical methods often lack direct connections to hydrogeological principles. More recently,  
125 machine learning (ML) and deep learning (DL) methodologies have gained significant promi-  
126 nence in hydrology and water resource applications (see Tripathy and Mishra (2024) for an  
127 overview on DL usage in hydrology). More specifically, physics-guided models, incorpo-  
128 rating geophysical knowledge into ML or DL models, can effectively handle and uncover  
129 hidden patterns in complex and high-dimensional datasets, and serve as a bridge between  
130 hydrogeology and geophysics. Abi Nader et al. (2023) combined ML and seismic monitoring  
131 to appraise punctual GWT levels with great precision, using raw seismic noise records. Cai  
132 et al. (2022) was able to estimate GWT levels with more accuracy with a physics-guided DL  
133 model than with a pure DL model, using water balance equations as a physical constraint.

134 This study takes advantage of a geologically well constrained sinkhole-affected site  
135 equipped with a dense geophone array and two piezometers. It offers almost a year of  
136 observed passive seismic data, revealing temporal trends that could be correlated with the  
137 GWT level seasonal variations. The objective of this study is to demonstrate the utility  
138 of DCs, obtained through passive seismic methods, in monitoring GWT levels. We intro-  
139 duce an innovative physics-guided DL method, coupling 2D passive-MASW and a MLP,  
140 to estimate daily 2D GWT maps from a single piezometer. After introducing the test site  
141 and providing a comprehensive overview of the passive-MASW survey geometry and data,  
142 we give a description of the method employed for building, training and testing the MLP.  
143 Subsequently, we showcase the generated 2D GWT maps resulting from the application of

144 this method, discuss the hydrogeological implications, and explore the limitations associated  
145 with such approach.

## 146 **2 Study site and data**

### 147 **2.1 A sensitive but well constraint site**

148 The study site is located along a railway line in the Grand-Est region of France (see  
149 Figure 1a,b) at the eastern edge of the Paris Basin. The site area has a stratigraphic com-  
150 position characterized by an 80-meter-thick cover formation, primarily composed of middle  
151 and lower Muschelkalk alluvium, clays, and marls originating from the middle Triassic pe-  
152 riod, underlayed by a substratum layer of lower Triassic sandstones (LTS). The hydrological  
153 context of this cover layer has not been studied at the local scale of the site. Only a large  
154 GWT map of the LTS aquifer from 2010 is available at the Lorraine region scale (Nguyen-  
155 Thé et al., 2010). At the acknowledgment of the authors, the connectivity of the cover layer  
156 alluvium aquifer with the LTS aquifer is not determined, and will not be discussed.

157 Between 1989 and 2017, this railway site has encountered several instances of sinkhole  
158 dropouts, particularly impacting the integrity of the railway on the southwest side towards  
159 the bridge (see Figure 1b). These sinkholes are attributed to gypsum dissolution in the  
160 marl layers. Consequently, a cement-based grout was injected at a depth of 20 m in the  
161 soil to reinforce the structure in 2018. Five Auger drilling tests with depths up to 20 m  
162 were conducted in December 2022 with the aim of detecting potential eventual cavities, as  
163 depicted in Figure 1b. These tests revealed no cavities and facilitated a visual characteri-  
164 zation of the various layers constituting the near-surface (see Figure 1c). An approximately  
165 10 m-thick layer of alluvium, consisting of a mixture of sand and clay, appears to overlay  
166 a denser layer of marly clays and highly compact marls. This observation aligns coherently  
167 with the expected geological composition of the middle and lower Muschelkalk layer.

### 168 **2.2 Monitoring setup and data**

169 To effectively address and mitigate the risks posed by sinkholes, a continuous ground  
170 monitoring through 2D passive-MASW using seismic noise induced by trains (Bardaine &  
171 Rondeleux, 2018; Bardainne et al., 2022; Tarnus et al., 2022a, 2022b; Bardainne et al.,  
172 2023), combined with two piezometers has been established as the best approach in late

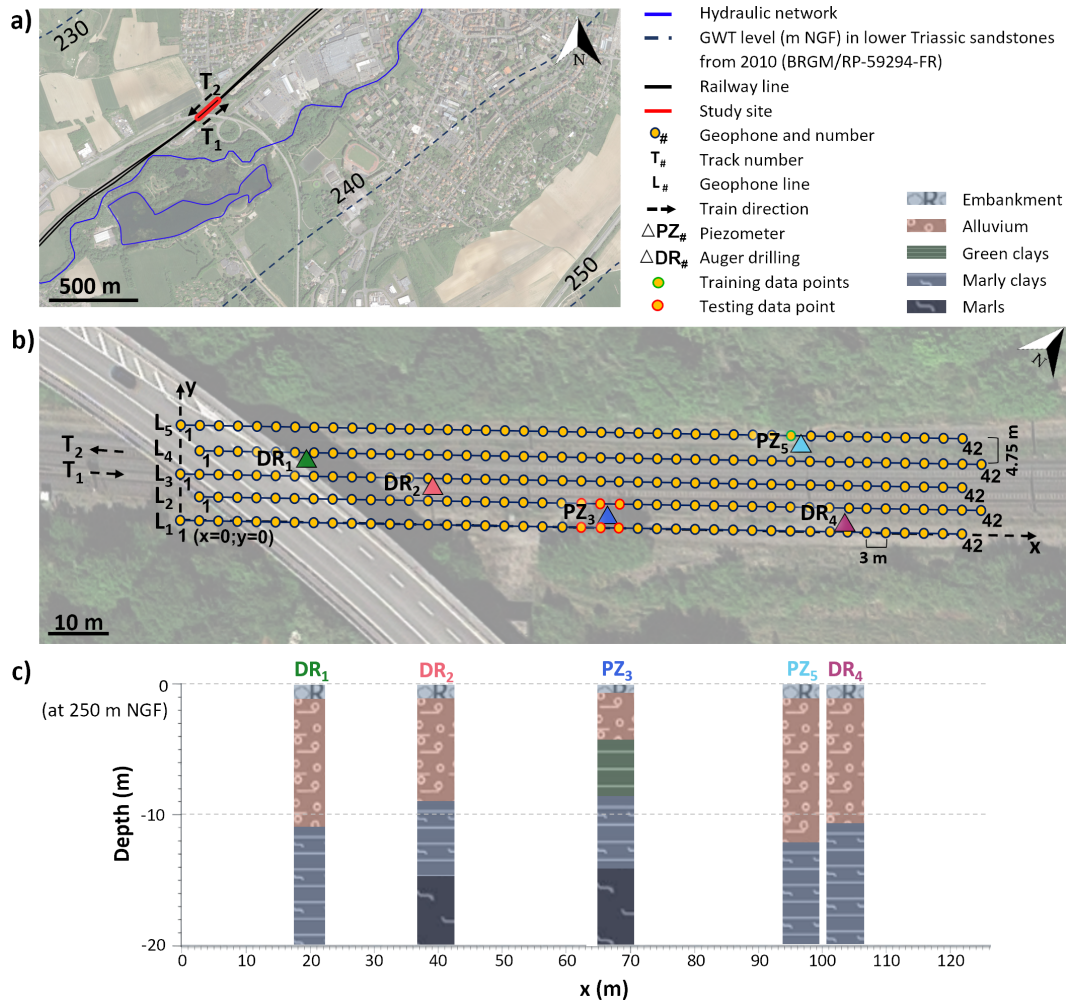


**Figure 1.** (a) Location map of the site with hydraulic networks and GWT levels of the lower Triassic sandstone aquifer. (b) Experimental design of the study site showing the five lines ( $L_1$  to  $L_5$ ) of 42 geophones (yellow dots), planted parallel to the railway tracks, and the track numbers ( $T_1$  and  $T_2$ ) with train directions.  $x$  and  $y$  correspond to the distance parallel and perpendicular to the railway tracks, respectively, and point  $(x = 0; y = 0)$  is at geophone 1 of array line 1 ( $L_1 - P_1$ ). Data points used for training and testing the MLP are colored in red around piezometer  $PZ_3$ , and green close to piezometer  $PZ_5$ , respectively.  $DR_1$ ,  $DR_2$ , and  $DR_4$  correspond to Auger drilling locations without piezometers. (c) Lithographic log at the 5 drillings. The lithology consists of an alluvial layer of sand and clay that is roughly 10 meters thick, overlying a denser section of marly clays and highly compact marls.

173 2020. Following the installation of the piezometers in late 2022, the studied period extends  
 174 from December 30, 2022, to September 3, 2023.

175 Passive seismic noise induced by train passages has been recorded using five uniform  
 176 linear arrays ( $L_1$  to  $L_5$  on Figure 1b), since September 2020. Each linear array has a  
 177 length of 123 m and is equipped with 42 3-meter spaced geophones. The geophones were  
 178 strategically positioned along the rail track, either on the cess (i.e., the track side) for linear  
 179 arrays  $L_1$  and  $L_5$ , or on the ballast for  $L_2$ ,  $L_3$ , and  $L_4$ . Daily DCs have been estimated  
 180 at each point of the array, covering a frequency range from 5 to 50 Hz., and resampled in  
 181 wavelengths ( $\lambda = V_R/f$ ) within the range of 4 to 15 m, with a step of 0.5 m.

182  $V_R$  variation over frequencies or wavelengths, seen in DCs, is linked to the medium's  
 183 shear velocity ( $V_S$ ) variation over depth. However, it's crucial to note that this transfor-  
 184 mation is nonlinear. Yet, wavelength resampling offers a more accurate link to depth in  
 185 comparison to frequencies, enabling precise targeting of the first meters of the near-surface.  
 186 Typically, the depth is around half or one-third of the wavelength (Shtivelman, 1999; Foti  
 187 et al., 2018). Therefore, this resampling should primarily target depths ranging from -1.5  
 188 to -5 m.

189 Figure 2 shows every estimated daily DC, from December 30, 2022, to September 3,  
 190 2023, sampled over frequencies and wavelengths, close to  $PZ_3$  at point 23 of geophone  
 191 line 1 ( $L_1$ - $P_{23}$ ), and close to  $PZ_5$  at point 33 of geophone line 5 ( $L_5$ - $P_{33}$ ) (see Figure 1b).  
 192 In Figure 3, examples of  $V_R$  pseudo-sections showcase the DCs sampled over wavelengths  
 193 along the 5 linear arrays, on April 1, 2023, and July 1, 2023, at high and low water periods,  
 194 respectively (see Figures 4a,b).  $V_R$  pseudo-sections over frequencies version is shown in  
 195 Figure A1 of Appendix A. Figures 2 and 3 reveal a spatial and temporal evolution of  $V_R$   
 196 that could be correlated with GWT geometry and dynamics. This indicates the potential  
 197 utility of employing this method for the ongoing monitoring purposes.

198 Both piezometers were equipped on December 30, 2022, at two of the five drilling loca-  
 199 tions, and have been recording daily GWT levels over time (see  $PZ_3$  and  $PZ_5$  in Figure 1b).  
 200 GWT level data at  $PZ_3$  and  $PZ_5$  is presented in Figures 4a and b. Both GWT levels are  
 201 situated within the alluvium layer (see Figure 1c). However, the two piezometers display  
 202 distinct behaviors.  $PZ_3$  is more responsive, and displays greater amplitude variations, in  
 203 comparison with  $PZ_5$ . Figures 4c and d show  $V_R$  variation over time for all wavelengths at  
 204 both piezometer locations. It's worth noting that the steep change in  $V_R$  at  $\lambda = 8$  m ob-

205 served in Figures 2c and 4c could correspond to the GWT level at  $PZ_4$ . However, conclusive  
 206 determination requires inversion of the DCs into  $V_S$  over depth models. Overall, despite the  
 207 differences in shape between DCs at the two piezometers (see Figures 2c and d), there seems  
 208 to be a correspondence with the observed trends in GWT level variations at array points  
 209 close to each piezometer. When GWT level decreases, there is a corresponding increase  
 210 in  $V_R$ , and conversely, when GWT level rises,  $V_R$  tends to decrease. The anti-correlated  
 211 variation is evident across all wavelengths at different scales, as depicted in Figures 4c and  
 212 d, and becomes even more pronounced when focusing on specific wavelengths in Figures 4e  
 213 and f. This inverse relationship between GWT levels and  $V_R$  is indicative of the influence of  
 214 groundwater dynamics on the spatial distribution and temporal evolution of  $V_R$ . Indeed, if  
 215 DCs demonstrate such anti-correlation with GWTs levels at these locations, then it is rea-  
 216 sonable to expect that this anti-correlation extends to every point along the seismic array.  
 217 We propose training a DL model using seismic and GWT level data from  $PZ_3$ , as it exhibits  
 218 the most pronounced responsiveness among the two piezometers. The goal is to be able to  
 219 translate DCs into GWT levels, and subsequently estimate GWT levels at the remaining  
 220 points along the entire array.

### 221 3 Method

#### 222 3.1 Multilayer Perceptron architecture

223 In this study, a MLP is used as a regression tool for estimating a GWT level from  
 224 a single DC, at several seismic array points and times. The MLP is the most basic feed-  
 225 forward artificial neural network and consists of multiple layers of fully connected neurons,  
 226 comprising an input layer, one or more hidden layers, and an output layer (Rosenblatt, 1958;  
 227 Murtagh, 1991). The use of a MLP allows for complex non-linear mappings between inputs  
 228 and outputs, making it particularly well-suited for capturing intricate relationships within  
 229 datasets.

230 A MLP with two hidden layers and  $k = 32$  neurons per layer was used in this applica-  
 231 tion (see Figure 5). The input and output layer sizes correspond to the number of features  
 232 of the input and output data. For each estimation, an unique DC of  $V_R$  resampled over  
 233 wavelengths ranging from 4 to 15 m and with a wavelength step of 0.5 m, is used as input,  
 234 which can be seen a vector  $\mathbf{x}$  of size  $n = 23$ . The output corresponds to an unique scalar

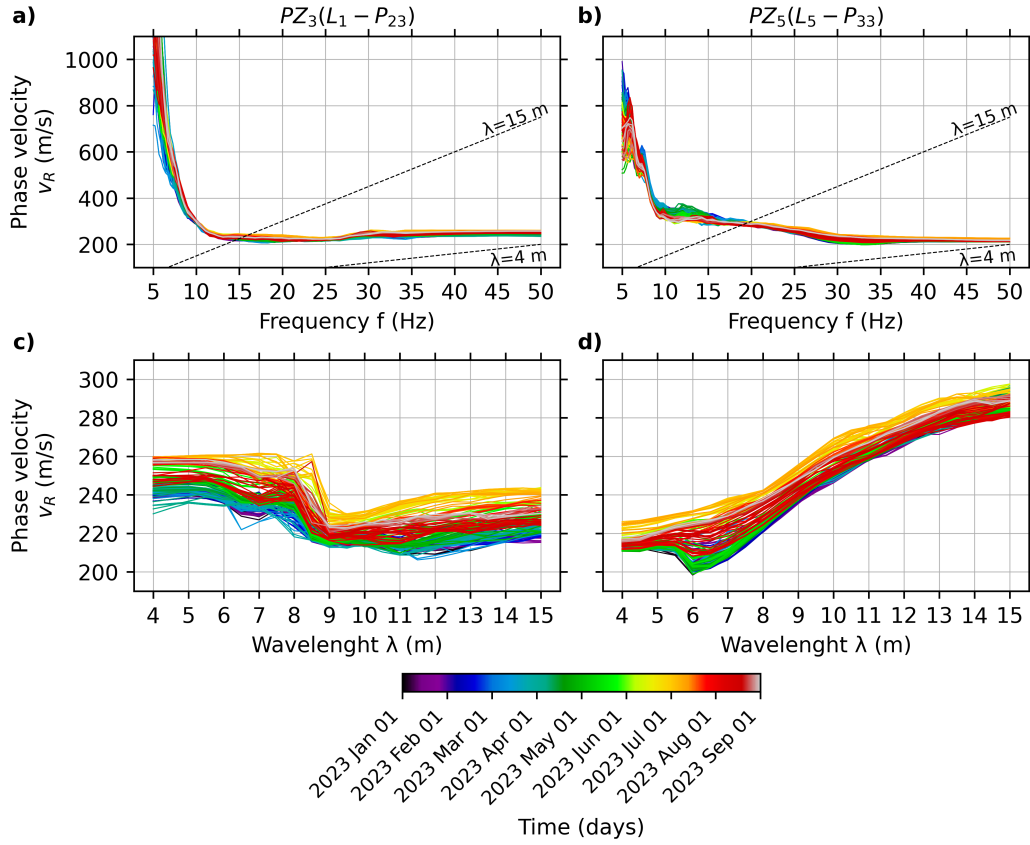


**Figure 2.** Time-series of raw dispersion curves over frequencies obtained (a) at seismic array point  $L_1 - P_{23}$ , close to piezometer  $PZ_3$ , and (b) at seismic array point  $L_5 - P_{33}$ , close to piezometer  $PZ_5$ . Resampled dispersion curves over wavelengths, ranging from  $\lambda = 4$  to  $\lambda = 15$  m, (c) at seismic array point  $L_1 - P_{23}$ , close to piezometer  $PZ_3$ , and (d) at seismic array point  $L_5 - P_{33}$ , close to piezometer  $PZ_5$  (see Figure 1b).

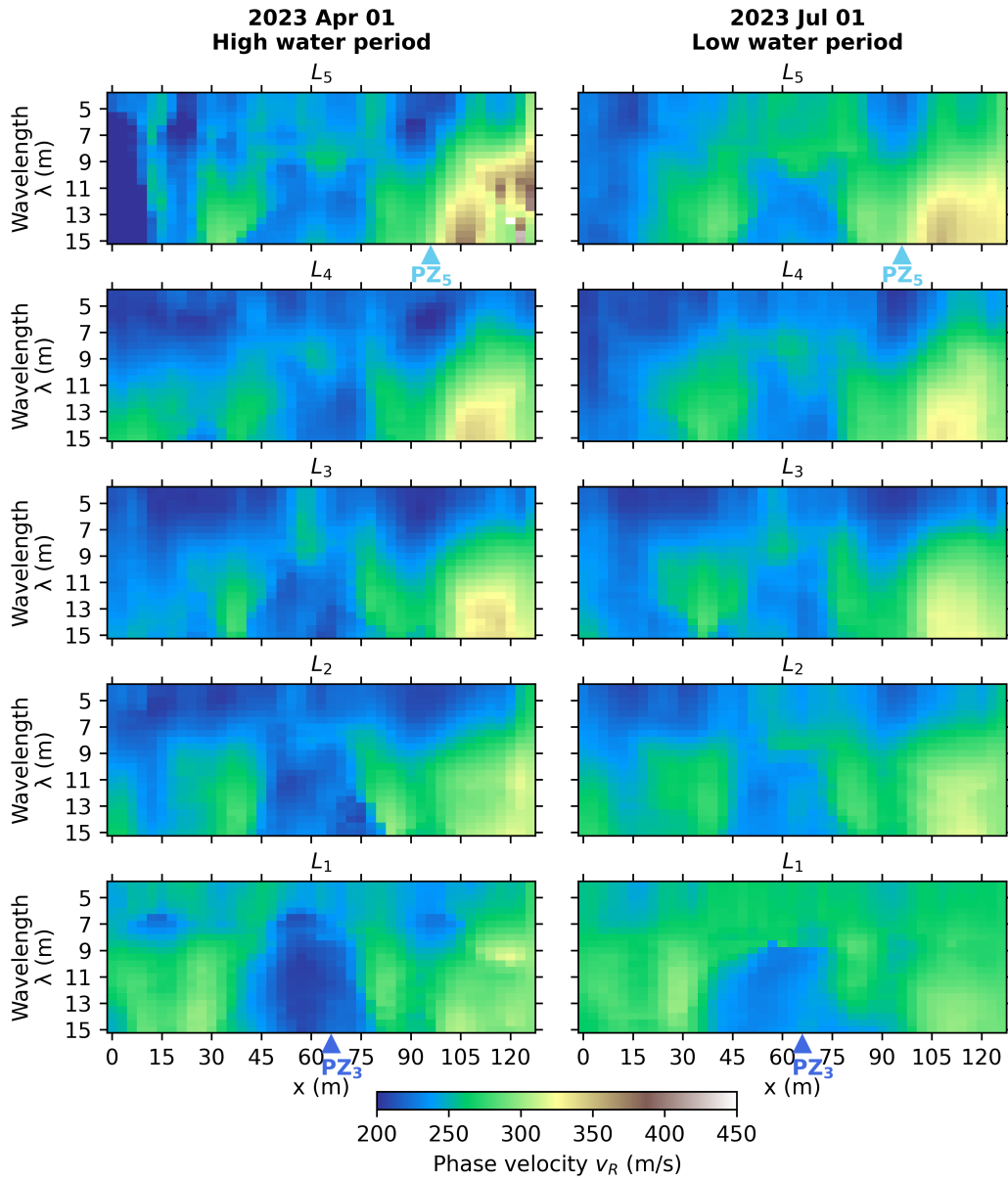


**Figure 3.**  $V_R$  pseudo-sections over wavelengths for the 5 linear geophone arrays ( $L_1$  to  $L_5$ ) (left) at a high water period on April 1, 2023, and (right) at a low water period on July 1, 2023. Positions of piezometers  $PZ_3$  and  $PZ_5$  are represented by the blue triangles on pseudo-sections  $L_1$  and  $L_5$ , respectively.

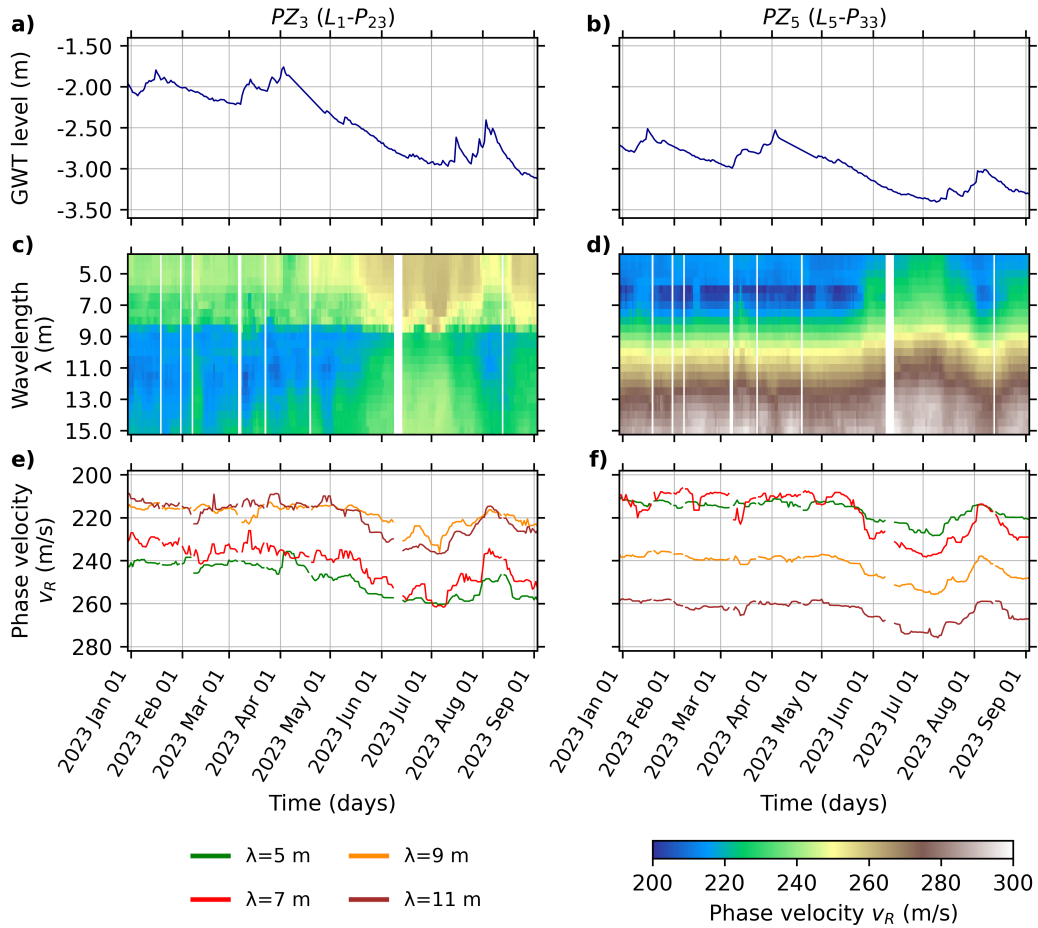


**Figure 4.** (a) and (b) Recorded GWT levels between December 30, 2022, and September 3, 2023, at  $PZ_3$  and  $PZ_5$ . (c) and (d)  $V_R$  over wavelengths evolution over the same time period at seismic array points  $L_1-P_{23}$ , close to  $PZ_3$ , and  $L_5-P_{33}$ , close to  $PZ_5$ . (e) and (f)  $V_R$  at wavelengths 5, 7, 9, and 11 m evolution over the same time period at seismic array points  $L_1-P_{23}$ , close to  $PZ_3$ , and  $L_5-P_{33}$ , close to  $PZ_5$ .

235  $y$  of an estimated GWT level. For each layer  $l$ , let  $\mathbf{w}^{(l)}$  be a vector of weights, initially  
 236 containing arbitrary values, and  $\mathbf{b}^{(l)}$  a vector of constants called "bias".

237 At the first layer  $l = 1$ , the perceptron calculates

$$z_j^{(1)} = b_j^{(1)} + \sum_{i=1}^n w_{ij}^{(1)} x_i, \quad (1)$$

238 for each neuron  $j$  over the  $k$  neurons of the first hidden layer, and with each feature  $i$  over  
 239 the  $n$  features of the input vector  $\mathbf{x}$ . Then, the vector  $\mathbf{z}^{(1)}$  goes through a *Rectified Linear*  
 240 *Unit* function *ReLU* introducing non-linearity to the model:

$$h_j^{(1)} = ReLu(z_j^{(1)}) = \begin{cases} z_j^{(1)} & \text{if } z_j^{(1)} > 0, \\ 0 & \text{otherwise.} \end{cases} \quad (2)$$

241 At the second layer  $l = 2$ , the perceptron calculates

$$z_j^{(2)} = b_j^{(2)} + \sum_{i=1}^k w_{ij}^{(2)} h_i^{(1)}, \quad (3)$$

242 for each neuron  $j$  over the  $k$  neurons of the second layer, and with each neuron  $i$  over the  
 243  $k$  neurons of the previous first hidden layer. Again, the vector  $\mathbf{z}^{(2)}$  goes through a *Rectified*  
 244 *Linear Unit* function *ReLU* :

$$h_j^{(2)} = ReLu(z_j^{(2)}) = \begin{cases} z_j^{(2)} & \text{if } z_j^{(2)} > 0, \\ 0 & \text{otherwise.} \end{cases} \quad (4)$$

245 Finally, at the output layer, the perceptron calculates

$$z_1^{(out)} = b_1^{(out)} + \sum_{i=1}^k w_{i1}^{(out)} h_i^{(2)}, \quad (5)$$

246 for the unique neuron of the output layer, and with each neuron  $i$  over the  $k$  neurons of the  
 247 previous second hidden layer. Finally,  $z^{(out)}$  goes through an *Identity* activation function  
 248 *linear*, which is the equivalent of no activation, to obtain the estimated scalar value  $y$ :

$$y = linear(z^{(out)}) = z^{(out)}. \quad (6)$$

### 249 3.2 Data preprocessing and training

250 The MLP goes through a training phase to optimize its performance and enhance its  
 251 ability to make accurate estimations. The training data involved daily DCs measurements  
 252 at specific seismic array points surrounding  $PZ_3$  ( $L_1-P_{22}$ ,  $L_1-P_{23}$ ,  $L_1-P_{24}$ ,  $L_2-P_{21}$ ,  $L_2-P_{22}$ ,  
 253 and  $L_2-P_{23}$ ) as inputs, and daily GWT level measurements at  $PZ_3$  as expected outputs.

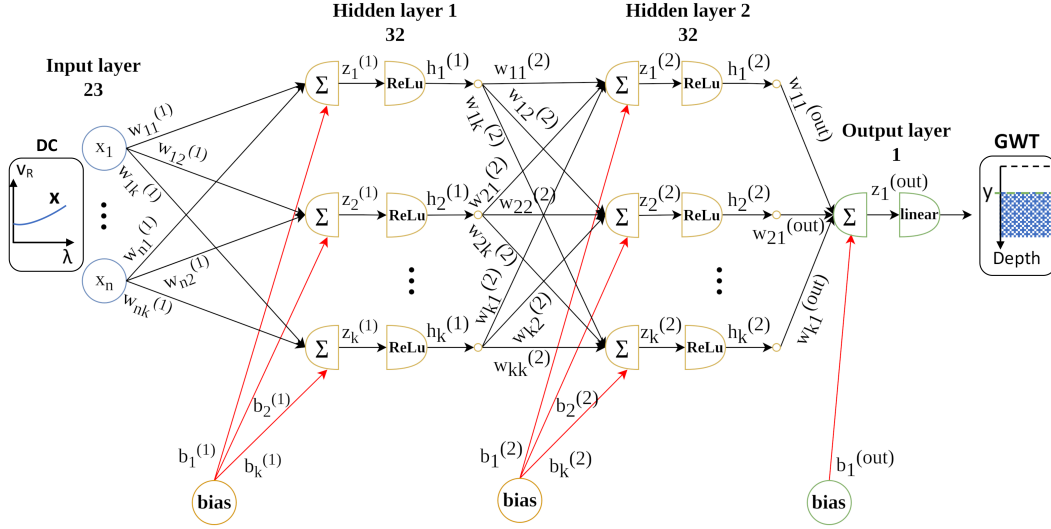


**Figure 5.** Multilayer perceptron with an input layer, two hidden layers, and an output layer. A DC ( $V_R$  over wavelength  $\lambda$ ) is used as input to predict a GWT level. The input vector  $\mathbf{x}$  has  $n = 23$  features, each hidden layer  $l$  has  $k = 32$  neurons, and the output  $y$  is a scalar.  $\mathbf{w}^{(l)}$  is a weight or leaning coefficient vector and  $\mathbf{b}^{(l)}$  a vector of constants called "bias". *ReLU* and *linear* are the *Rectified Linear Unit* and *Identity* activation functions.

254 Thus, for an unique day and a unique GTW level output, six different inputs are used,  
 255 corresponding to the closest six points around the piezometer. Due to the similarity of the  
 256 DCs at these points, this allows for a better spatial versatility of the model, and can be seen  
 257 as data augmentation (Shorten & Khoshgoftaar, 2019). To facilitate the training phase, DCs  
 258 were normalized by 2000 (i.e., around twice the maximum observed  $V_R$ ) and GWT levels  
 259 were used in absolute numbers. This data collection spanned from December 30, 2022, to  
 260 September 3, 2023, encompassing a total of 248 days. Days without data due to technical  
 261 issues were excluded from the dataset.

262 During the training process, weights and biases are refined to minimize the difference  
 263 between estimated outputs and actual target values. The training begins with the pre-  
 264 sentation of training data, with known input and outputs, to the MLP. Subsequently, the  
 265 calculated errors in terms of *root-mean-square error* (RMSE) of the resulting estimations are  
 266 backpropagated through the network (Rosenblatt, 1958; Linnainmaa, 1976; Werbos, 1982).  
 267 This involves adjusting the weights and biases in the opposite direction of the error gradient.  
 268 In this study, the magnitude of these adjustments was determined by a stochastic gradient  
 269 descent *Adam* optimization algorithm with a learning rate of  $10^{-4}$ , which fine-tunes the

270 model iteratively (Kingma & Ba, 2014). This iterative adjustment process was done until  
 271 the MLP converges to a state where further refinement did not significantly improve its  
 272 estimation capabilities. The desired outcome was a trained MLP with optimized internal  
 273 parameters enabling it to generalize well to new, unseen data, making accurate estimations  
 274 in various scenarios.

275 A maximum of 1000 training epochs (i.e., iterations) with 2 samples per gradient  
 276 update were done. Daily DCs measurements at seismic array points surrounding  $PZ_5$  ( $L_4$ -  
 277  $P_{31}$ ,  $L_4$ - $P_{32}$ ,  $L_4$ - $P_{33}$ ,  $L_5$ - $P_{32}$ ,  $L_5$ - $P_{33}$ , and  $L_5$ - $P_{34}$ ), and GWT levels at  $PZ_5$  were used as  
 278 a validation dataset for "early-stopping", to limit the number of epochs and avoid model  
 279 overfitting (Ying, 2019; Tripathy & Mishra, 2024).

## 280 4 Results

281 Figure 6 compares the GWT levels observed at  $PZ_3$  and  $PZ_5$  with the estimations  
 282 at seismic array points  $L_1$ - $P_{23}$  close to  $PZ_3$ , and  $L_5$ - $P_{33}$  close to  $PZ_5$ , between December  
 283 30, 2022, and September 3, 2023. As anticipated, the estimated and observed values for  
 284  $PZ_3$ , which was used in the training process, show a close proximity (see Figures 6a and  
 285 b), with an RMSE of 0.03 m and a *coefficient of determination*  $R^2$  of 80 % (see Appendix  
 286 D for definitions). Please note that this score could possibly be higher but is limited to  
 287 able a great generalization of the model. While the model successfully captures the general  
 288 patterns, it exhibits minor fluctuations that deviate from the observed values. Despite these  
 289 slight deviations, the overall agreement between estimated and observed values underscores  
 290 the model's capability to replicate the general trends associated with  $PZ_3$ . The model  
 291 also demonstrates its ability to accurately extrapolate and estimate GWT levels at  $PZ_5$ ,  
 292 a location not included in the training set (see Figures 6c and d). Estimations for  $PZ_5$   
 293 yield a RMSE of 0.03 m and a  $R^2$  of 68%, suggesting a low level of estimation error and a  
 294 high degree of accuracy. However, GWT levels are slightly overestimated by 25 cm between  
 295 May and June 2023 and between August and September 2023. These errors could certainly  
 296 be corrected by extending the time span of groundwater table (GWT) level data used for  
 297 training, a limitation imposed by the time-frame of this research.

298 Figures 7b-i show 2D GWT maps with estimations made at each seismic array point,  
 299 at the beginning of January, February, April, May, June, July, August, and September,  
 300 2023. Estimated GWT levels at the five drilling locations, are highlighted in Figure 7a.

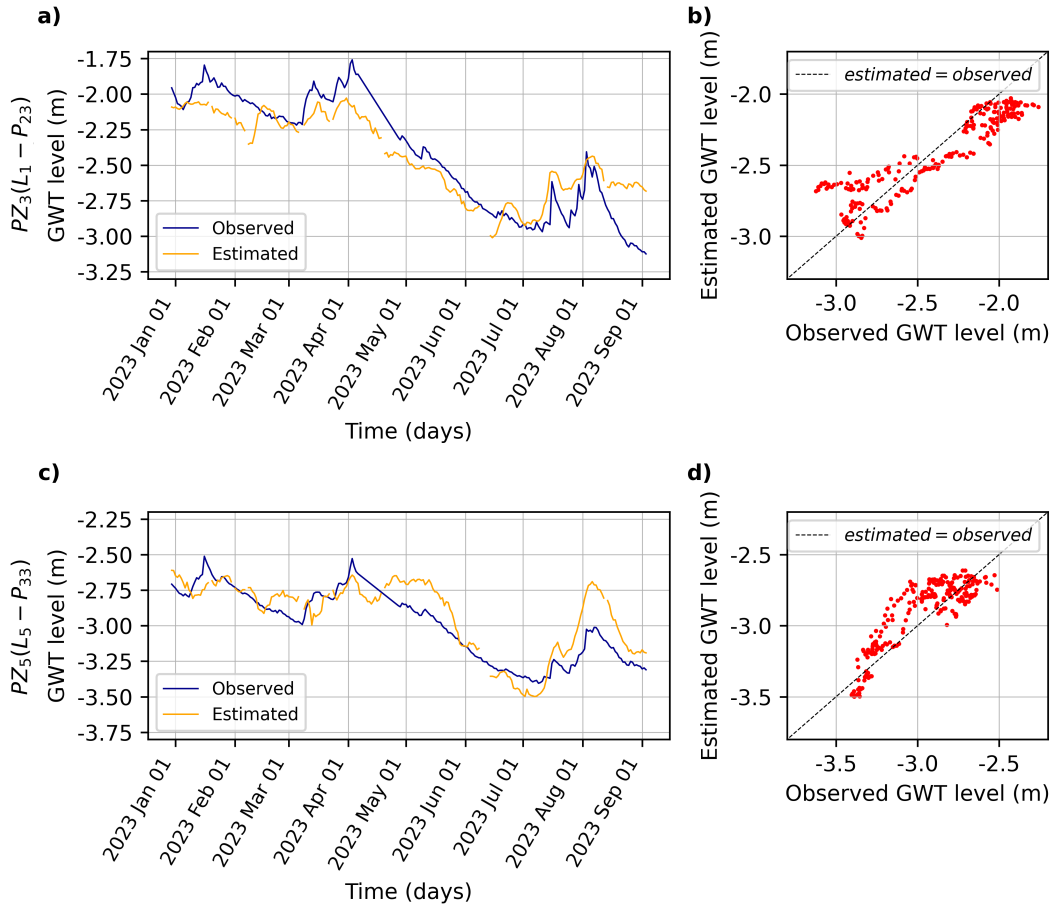


**Figure 6.** MLP's GWT level estimations, obtained using DCs at seismic array points around  $PZ_3$  ( $L_1-P_{22}$ ,  $L_1-P_{23}$ ,  $L_1-P_{24}$ ,  $L_2-P_{21}$ ,  $L_2-P_{22}$ , and  $L_2-P_{23}$ ) and observed GWT levels at  $PZ_3$  as training data. (a) GWT level over time observed at  $PZ_3$  and estimated at seismic array point  $L_1-P_{23}$ . (b) GWT levels observed at  $PZ_3$  versus estimated at  $L_1-P_{23}$ . (c) GWT level over time observed at  $PZ_5$  and estimated at seismic array point  $L_5-P_{33}$ . (d) GWT levels observed at  $PZ_5$  versus estimated at point  $L_5-P_{33}$ .

301 The GWT maps exhibit a noticeable global variation, approximately 1 m, between the high  
 302 water period (April 2023) and the low water period (July 2023) (see Figure 8). Nevertheless,  
 303 a spatial heterogeneity over  $x$  and  $y$  is evident, revealing zones with relatively both high  
 304 and low GWT levels. More specifically, the area between  $x = 0$  and  $x = 20$  m, comprising  
 305  $DR_1$  and  $DR_2$ , consistently exhibits elevated levels at around -2 m, with minimal variation  
 306 over time. This region corresponds to the 20-meter deep grout-injected zone. The area  
 307 between  $x = 30$  and  $x = 60$  m, encompassing  $PZ_3$ , and between  $x = 80$  and  $x = 90$  m,  
 308 encompassing  $PZ_5$ , demonstrate elevated levels from January to May 2023. However, a  
 309 noticeable decline is observed during the summer months. In the central area of the map, a  
 310 small low-level zone with minimal variation over time, enclosed by a high-level zone, can be  
 311 noticed. Regions between  $x = 20$  and  $x = 30$  m, and between  $x = 60$  and  $x = 80$  m, exhibit  
 312 relatively low GWT levels. Additionally, the zone between  $x = 90$  and  $x = 126$  m, which  
 313 includes  $DR_4$ , displays the lowest GWT levels. For reference, this zone also registered the  
 314 highest values of  $V_R$  (see Figure 2). Artifacts exhibiting very high GWT level estimations  
 315 (between 0 and -1 m) and very low GWT level estimations (around -6 m) can be observed  
 316 at the border of the maps, along geophone line  $L_5$ , between February and May 2023 (see  
 317 Figures 7c,d,e). These artifacts are also observed in the raw  $V_R$  input data and were likely  
 318 initially induced during the computation and picking of the DCs.

## 319 5 Discussion

### 320 5.1 Geologic interpretation

321 Spatial and temporal variations in GWT levels observed in Figures 7 and 8 could be  
 322 explained by differences in lithology over the studied site, effectively captured by seismic  
 323 data. Areas with elevated GWT levels may be attributed to the presence of highly im-  
 324 permeable materials below alluvium, such as grout or clay. In such case, GW is impeded  
 325 from infiltrating into the subsurface, contributing to the observed elevated GWT levels. Ar-  
 326 eas exhibiting consistently high GWT levels with minimal variation could be attributed to  
 327 the presence of shallow, highly impermeable materials, such as clay, beneath the alluvium  
 328 layer. Areas with high GWT levels during high-water periods, and low GWT levels during  
 329 low-water periods, could be attributed to the presence of a deeper highly impermeable ma-  
 330 terial beneath alluvium. Conversely, areas with constant low GWT levels may be associated  
 331 with more permeable materials beneath alluvium. Figure 9 shows the GWT cross-section  
 332 traversing through all five drilling points, for different months along the year, accompanied

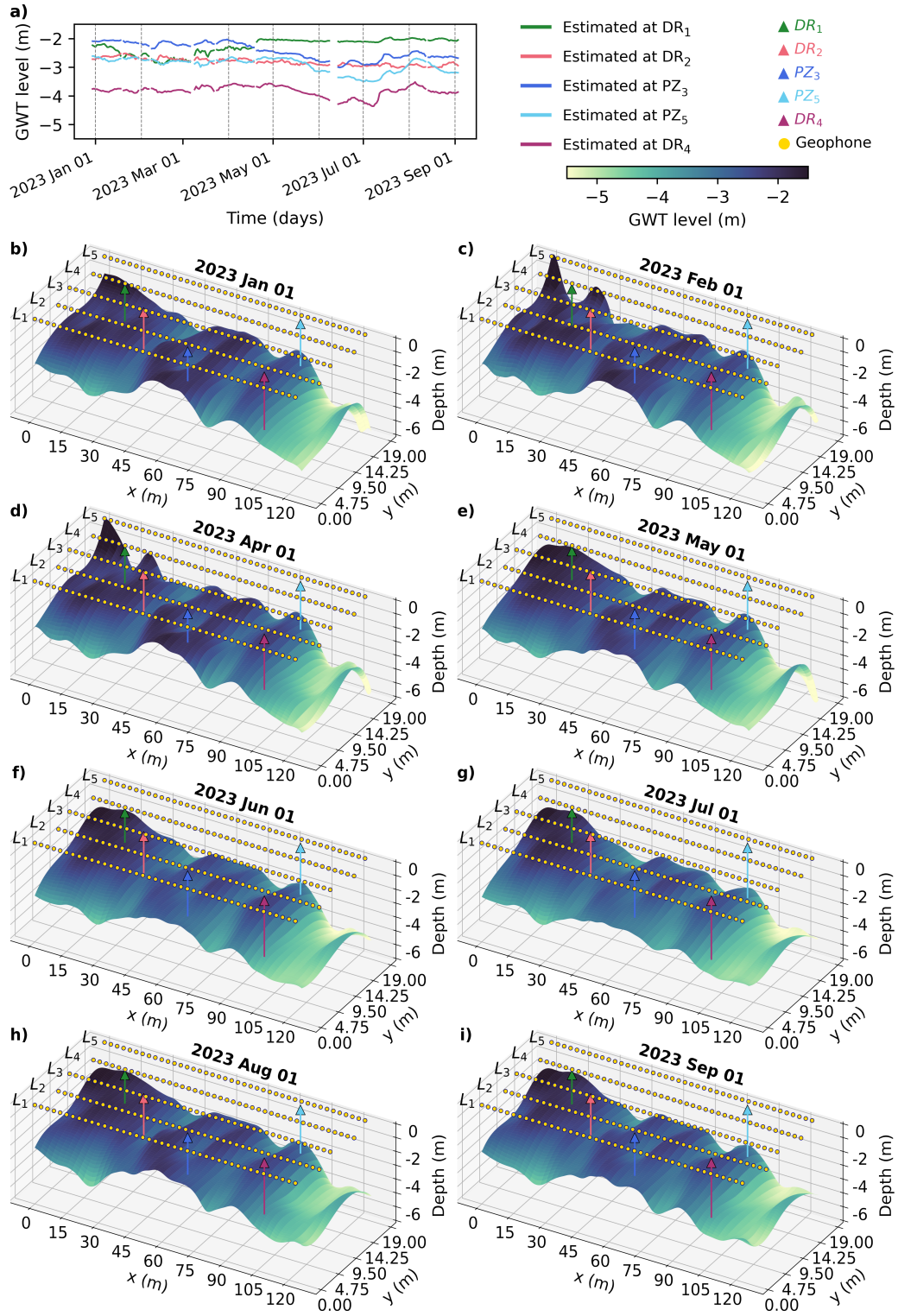


**Figure 7.** MLP’s GWT level estimations, obtained using DCs at seismic array points around  $PZ_3$  ( $L_1$ - $P_{22}$ ,  $L_1$ - $P_{23}$ ,  $L_1$ - $P_{24}$ ,  $L_2$ - $P_{21}$ ,  $L_2$ - $P_{22}$ , and  $L_2$ - $P_{23}$ ) and observed GWT levels at  $PZ_3$  as training data. (a) Estimated GWT levels over time at the five drilling and piezometers locations. (b) to (i) Estimated GWT level 2D maps at different dates, with geophone linear array ( $L_{\#}$ ), piezometer ( $PZ_{\#}$ ) and drilling ( $DR_{\#}$ ) positions at the surface.

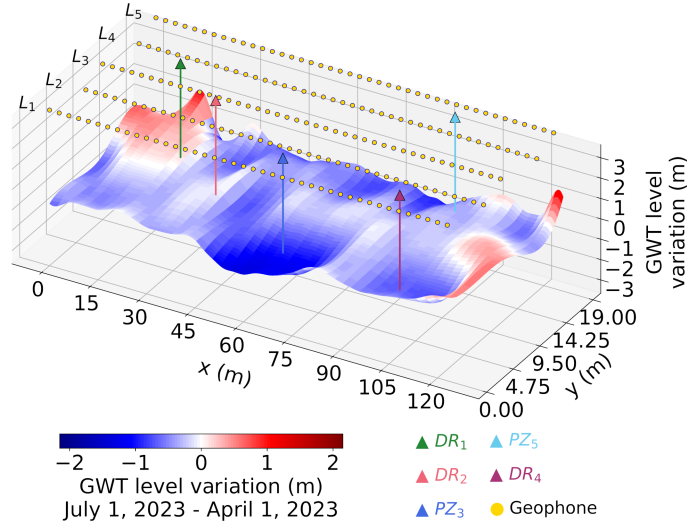


**Figure 8.** Estimated GWT level 2D map variation between high water period (April 1, 2023) and low water period (July 1, 2023), obtained using DCs at seismic array points around  $PZ_3$  ( $L_1$ - $P_{22}$ ,  $L_1$ - $P_{23}$ ,  $L_1$ - $P_{24}$ ,  $L_2$ - $P_{21}$ ,  $L_2$ - $P_{22}$ , and  $L_2$ - $P_{23}$ ) and observed GWT levels at  $PZ_3$  as training data. Geophone, piezometer and drilling positions are displayed at surface.

333 by geological logs illustrating the nature of the materials encountered. As expected, the  
 334 GWT is higher with greater variation above the shallow clay layer (drilling at  $PZ_3$ ). Be-  
 335 tween  $DR_2$  and  $PZ_3$ , close to  $DR_2$ , as well as between  $PZ_3$  and  $PZ_5$ , there is a decrease in  
 336 the GWT, with a distinctive pinching point. This could be explained by a transition from  
 337 highly impermeable to more permeable materials. All this suggests that zones  $x = 30$  and  
 338  $x = 60$  m, and between  $x = 80$  and  $x = 90$  m in a lesser degree, present a shallow clay layer.

## 339 5.2 Model robustness

340 Pseudo-sections of  $V_R$  over wavelengths for the five geophone array lines, computed  
 341 during the high water period (April 1, 2023) and the low water period (June 1, 2023),  
 342 and displayed in Figure 2, were inverted into sections of  $V_S$  over depth (see Figure 10 and  
 343 Figure C1 in Appendix C). Remarkably, on the five sections, the estimated GWT levels  
 344 align perfectly with a low-velocity layer (blue on Figure 10) characterized by a  $V_S$  between  
 345 200 and 250 m/s during these two periods. This alignment supports the credibility of the  
 346 method, as the MLP successfully estimated the depth of this layer despite the absence of  
 347 direct depth information in DCs. It is noteworthy that the GWT is closer to the surface  
 348 where this low-velocity layer is shallower and exhibits lower  $V_S$  values. Around  $x = 60$

on  $L_1$ , this low-velocity layer is placed just above the observed clay layer at drilling point  $PZ_3$ . This observation strongly supports the hypothesis that the low-velocity layer might be associated with saturated alluvium, and that its depth is influenced by the presence of an underlying clay layer. Conversely, zones with higher  $V_S$  also show lower GWT levels that seem to follow deep low-velocity layer, implying deeper saturated alluvium. This aligns with the absence of clay observed in the drillings and indicating a deeper interface between alluvium and the impermeable underlying marl layer.

To assess the influence of the number of piezometers on the estimated GWT level maps, a model was trained using data points around  $PZ_3$  ( $L_1$ - $P_{22}$ ,  $L_1$ - $P_{23}$ ,  $L_1$ - $P_{24}$ ,  $L_2$ - $P_{21}$ ,  $L_2$ - $P_{22}$  and  $L_2$ - $P_{23}$ ) and  $PZ_5$  ( $L_4$ - $P_{31}$ ,  $L_4$ - $P_{32}$ ,  $L_4$ - $P_{33}$ ,  $L_5$ - $P_{32}$ ,  $L_5$ - $P_{33}$  and  $L_5$ - $P_{34}$ ). The results, presented in Appendix B (see Figures B1, B2, B3, B4, and B5), reveal an enhanced estimation performance at both  $PZ_3$  ( $R^2$  of 88% and an RMSE of 0.01 m) and  $PZ_5$  ( $R^2$  of 72% and an RMSE of 0.01 m). Upon comparing the estimated GWT maps in Figures 7 (MLP trained with only  $PZ_3$ ) and B2 (MLP trained with both  $PZ_3$  and  $PZ_5$ ), it is evident that extreme high and low GWT level values appear to have been smoothed or flattened. Nevertheless, the general GWT levels and behavior remain highly consistent with the previous estimations. This supports the robustness of using an unique piezometer for training. However, employing multiple piezometers for different lithologies enhances the precision and stability of the method.

## 6 Conclusions

This study introduces a physics-guided DL model, combining 2D passive-MASW with a MLP, that estimates daily 2D GWT maps from a single piezometer. This hybrid approach offers an effective mean of monitoring GWTs with both spatial and temporal precision. The method exhibits notable generalization capabilities, with the ability to spatially extrapolate GWT level maps beyond the training dataset. Analysis of GWT maps reveals spatial and temporal variations, offering a nuanced understanding of GWT geometry and dynamics, and revealing valuable hydrogeological insights. The model successfully captures variations associated with lithological changes, demonstrating its efficacy in characterizing subsurface materials. In addition, the estimated GWT levels align closely with low-velocity layers, in terms of  $V_S$ , indicative of saturated alluvium and shallow clay layers. However, while the study demonstrates promising results, it is crucial to acknowledge its limitations. The model's performance may be influenced by site-specific conditions, and further validation

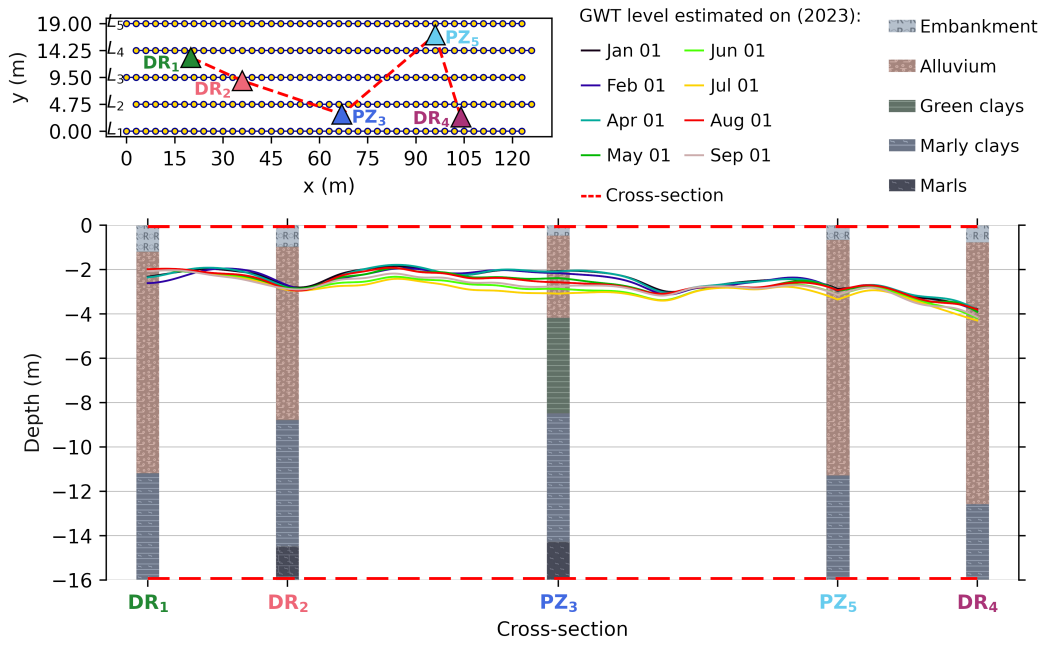


**Figure 9.** (a) Geophone array map and cross-section line (in red) between drilling and piezometers. (b) Cross-section of estimated GWT levels at different dates, obtained using DCs at seismic array points around  $PZ_3$  ( $L_1-P_{22}$ ,  $L_1-P_{23}$ ,  $L_1-P_{24}$ ,  $L_2-P_{21}$ ,  $L_2-P_{22}$ , and  $L_2-P_{23}$ ) and observed GWT levels at  $PZ_3$  as training data, with geologic logs illustrating the nature of the underground materials.

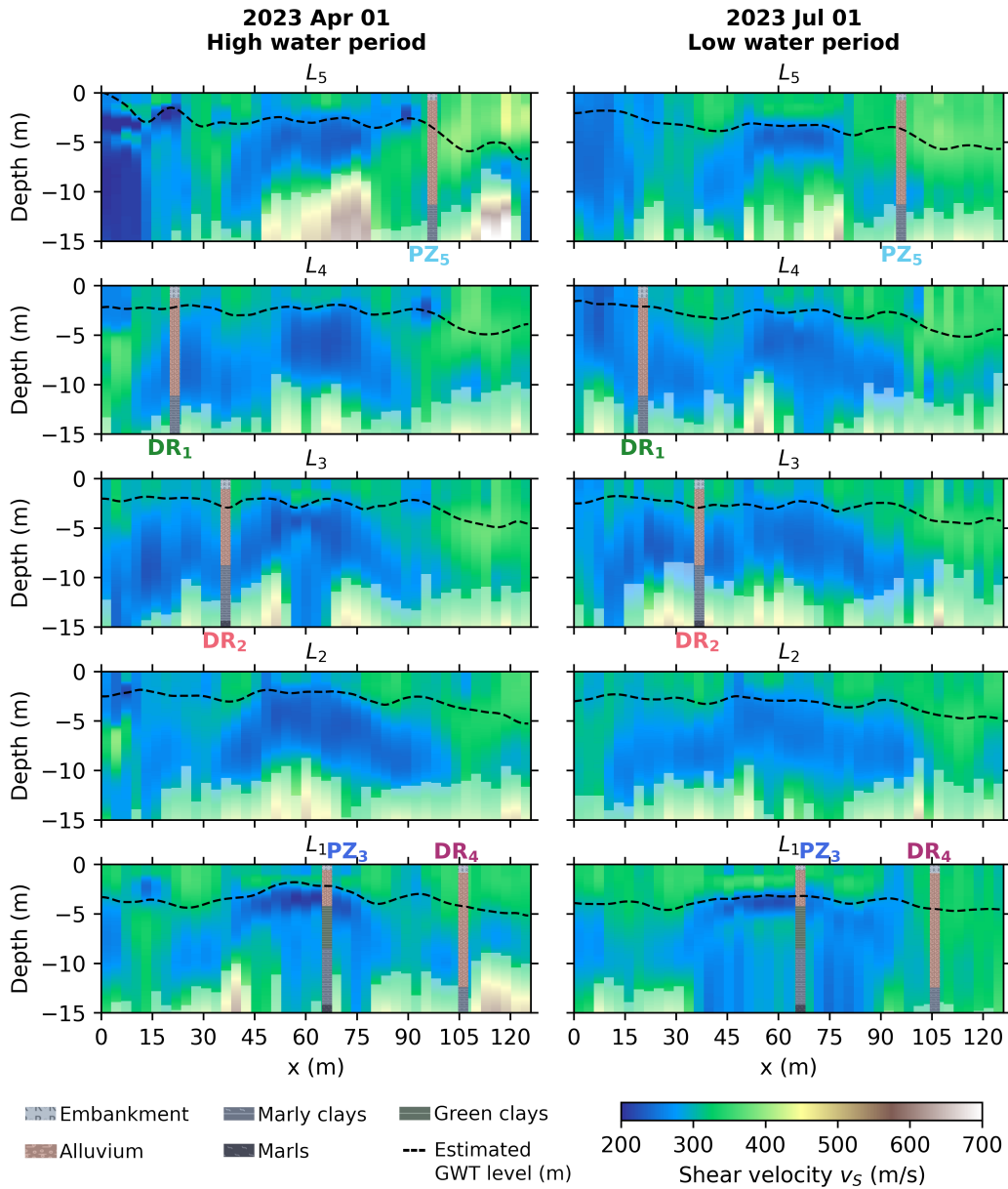


**Figure 10.** Inverted  $V_S$  sections over depth for the 5 linear geophone arrays ( $L_1$  to  $L_5$ ) at a high water period (April 1, 2023) and at a low water period (July 1, 2023). The white mask indicates depths where the standard deviation, between the mean  $V_S$  model and all other accepted models during inversion, is greater than 400 m/s. Estimated GWT levels, obtained using DCs at seismic array points around  $PZ_3$  ( $L_1$ - $P_{22}$ ,  $L_1$ - $P_{23}$ ,  $L_1$ - $P_{24}$ ,  $L_2$ - $P_{21}$ ,  $L_2$ - $P_{22}$ , and  $L_2$ - $P_{23}$ ) and observed GWT levels at  $PZ_3$  as training data, and geologic logs, illustrating the nature of the underground materials at five drilling coordinates, are superposed for interpretation.

381 across diverse geological settings is needed. By leveraging geophysical data and DL, the  
382 study contributes to advancing our understanding of subsurface dynamics and offers prac-  
383 tical insights for effective GW management and risk mitigation strategies. This integrated  
384 approach can be applied to monitor aquifer resilience at different scales, contribute to in-  
385 formed decision-making in the context of water resource management, and assess potential  
386 hazards such as sinkholes.

## 387 **Open Research Section**

388 All authors approved the final version of this article. Input data files and Python  
389 scripts used for the GWT level estimations are available on the online Zenodo repository  
390 (<https://doi.org/10.5281/zenodo.10854339>) and on the GitHub repository ([https://github.com/JoseCunhaTeixeira/GWT\\_prediction](https://github.com/JoseCunhaTeixeira/GWT_prediction)).  
391

## 392 **Acknowledgments**

393 This research was made possible through funding from SNCF Réseau, CNRS, Sorbonne Uni-  
394 versité, Mines Paris-PSL research contract, and the ANRT/Cifre-SNCF Réseau n°2021/1552  
395 convention. It is essential to acknowledge the contribution of the team involved in acquiring  
396 and processing the geophysical passive-MASW data. The successful execution of this study  
397 owes much to the efforts of the SERCEL Company, and particularly to the dedicated indi-  
398 viduals Thomas Bardainne, Renaud Tarnus, Nicolas Deladerriere, Ceifang Cai, Loic Michel,  
399 Lilas Vivin, and Helene Toubiana Lille. The authors also express gratitude to the local teams  
400 from SNCF Réseau their invaluable assistance and support, notably to Fabrice Pierron for  
401 all the GIS cartography. The deep learning model was coded using Python package *Keras*  
402 (Chollet et al., 2015). Dispersion curve inversions were conducted using the open-source  
403 software package *SWIP*<sup>1</sup> implemented by Pasquet and Bodet (2017).

---

<sup>1</sup> <https://github.com/spasquet/SWIP>

404 **Appendix A Raw data**

405 Figure A1 shows the same  $V_R$  pseudo-sections presented in Figure 2, at a high water  
 406 period on April 1, 2023, and at a low water period on July 1, 2023, but with DCs sampled  
 407 over frequencies ranging from 5 to 50 Hz.

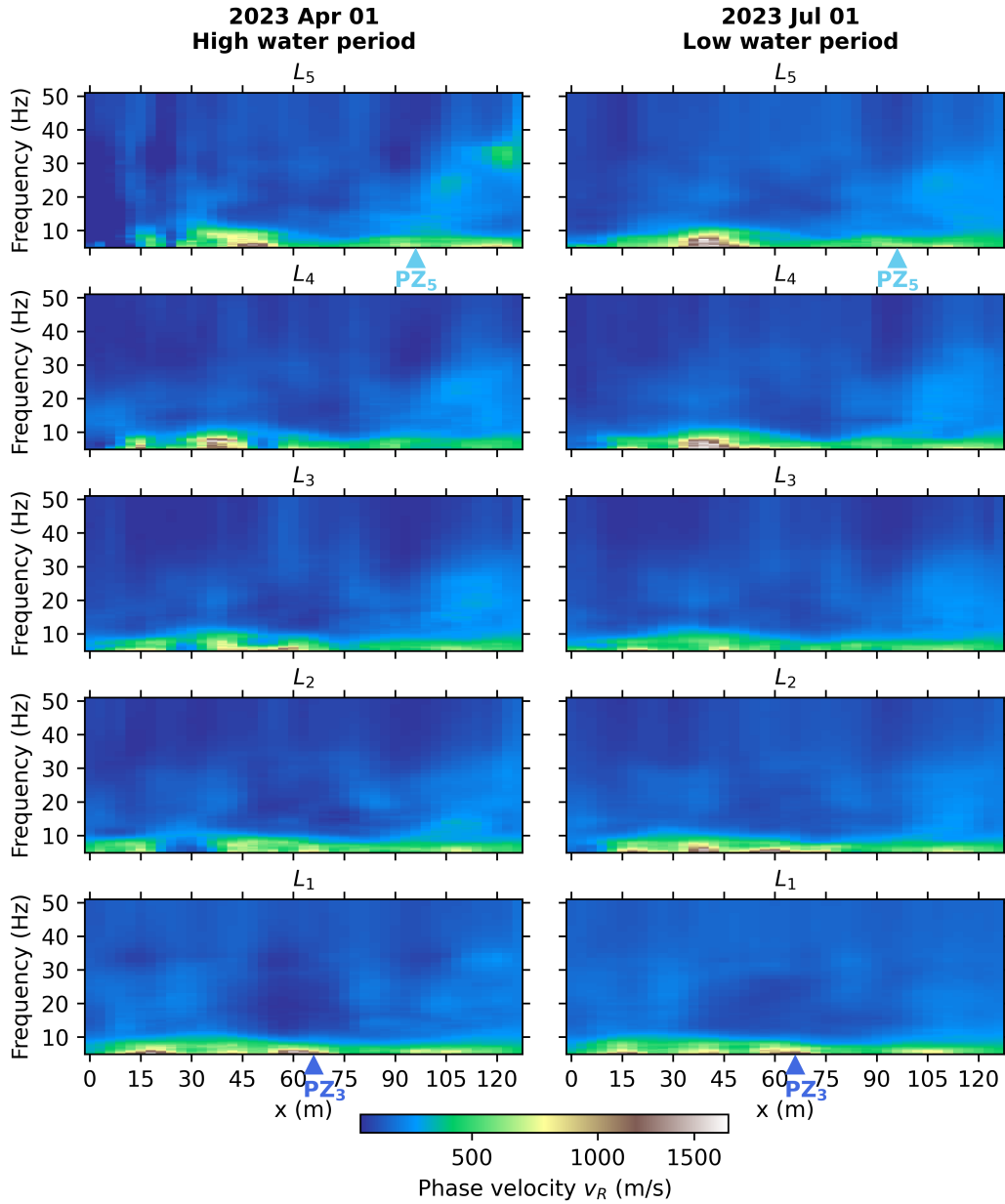


**Figure A1.**  $V_R$  pseudo-sections over frequencies for the 5 linear geophone arrays ( $L_1$  to  $L_5$ ) (left) at a high water period on April 1, 2023, and (right) at a low water period on July 1, 2023. Positions of piezometers  $PZ_3$  and  $PZ_5$  are represented by the blue triangles on profiles  $L_1$  and  $L_5$ , respectively.

**408 Appendix B Model trained with both piezometers**

409 In this section, we present the same study, but incorporating results from a MLP  
410 model trained using seismic and GWT level data from both piezometers. The expanded  
411 dataset enhances the model's training with a more comprehensive understanding of the  
412 subsurface dynamics at multiple locations. By integrating seismic and GWT data from  
413 both piezometers, we aim to provide a more robust and nuanced analysis of the GWT  
414 variations and their correlation with the subsurface characteristics. Results are similar to  
415 those obtained using a single piezometer for training, and are discussed in Section 5.

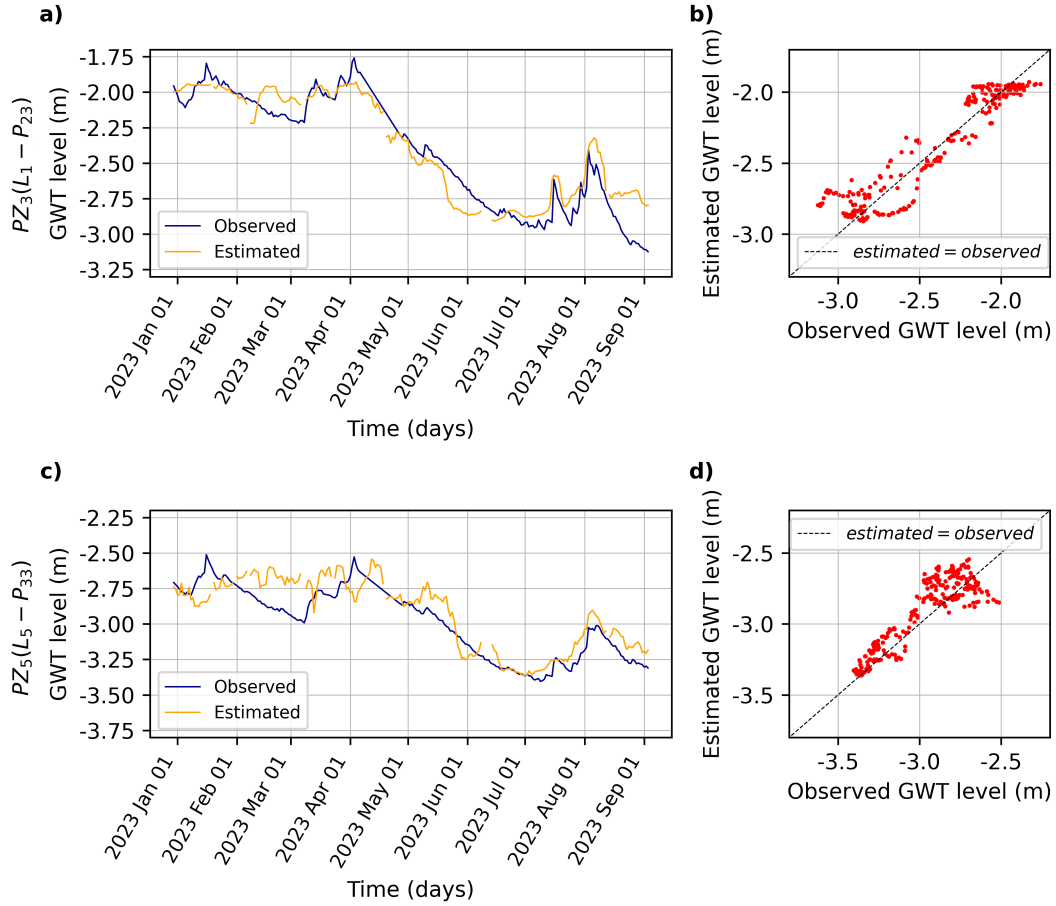


**Figure B1.** MLP's GWT level estimations, obtained using DCs at seismic array points around  $PZ_3$  ( $L_1-P_{22}$ ,  $L_1-P_{23}$ ,  $L_1-P_{24}$ ,  $L_2-P_{21}$ ,  $L_2-P_{22}$ , and  $L_2-P_{23}$ ) and  $PZ_5$  ( $L_4-P_{31}$ ,  $L_4-P_{32}$ ,  $L_4-P_{33}$ ,  $L_5-P_{32}$ ,  $L_5-P_{33}$ , and  $L_5-P_{34}$ ), and observed GWT levels at  $PZ_3$  and  $PZ_5$  as training data. (a) GWT level over time observed at  $PZ_3$  and estimated at seismic array point  $L_1-P_{23}$ . (b) GWT levels observed at  $PZ_3$  versus estimated at  $L_1-P_{23}$ . (c) GWT level over time observed at  $PZ_5$  and estimated at seismic array point  $L_5-P_{33}$ . (d) GWT levels observed at  $PZ_5$  versus estimated at point  $L_5-P_{33}$ .

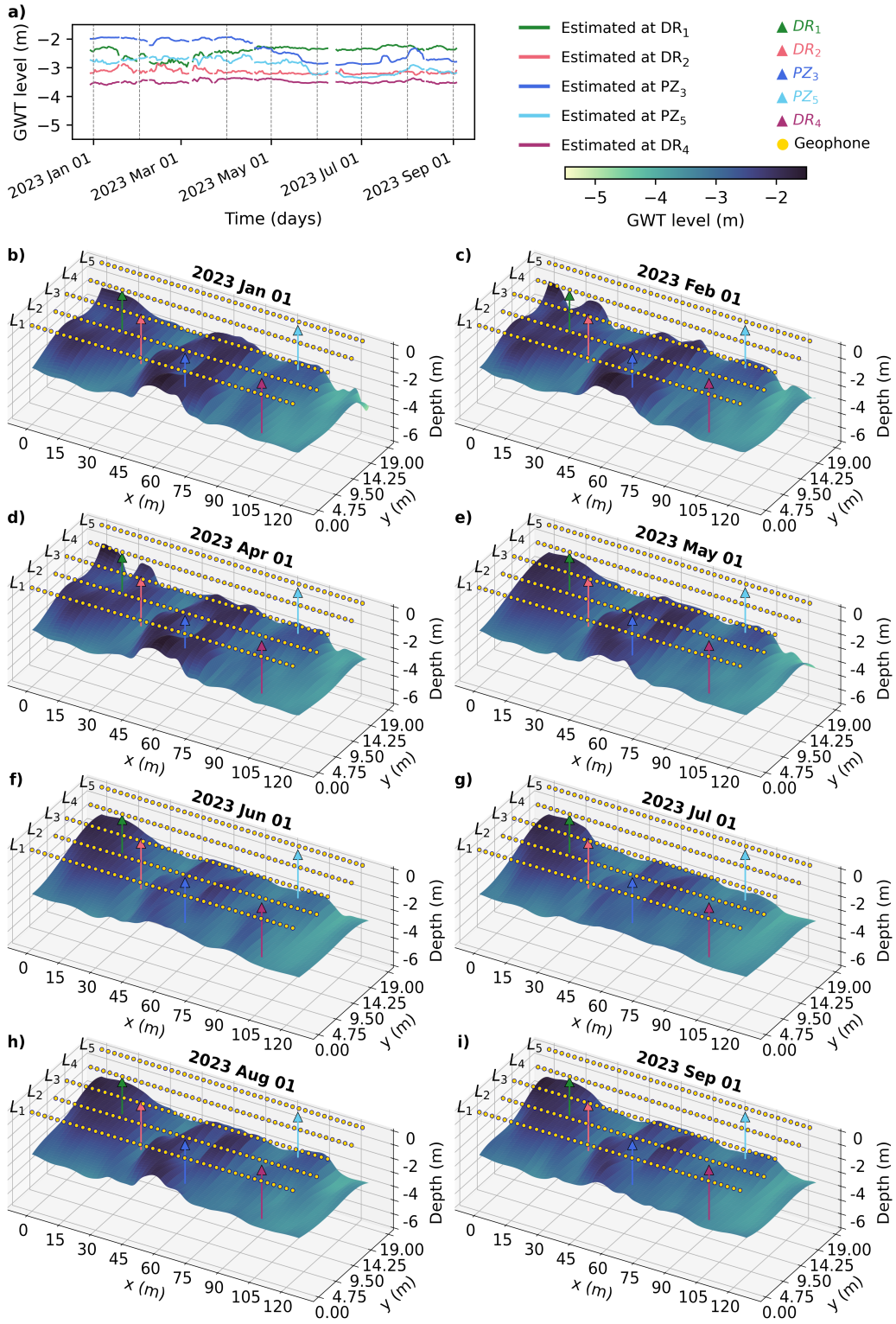


**Figure B2.** MLP's GWT level estimations, obtained using DCs at seismic array points around  $PZ_3$  ( $L_1$ - $P_{22}$ ,  $L_1$ - $P_{23}$ ,  $L_1$ - $P_{24}$ ,  $L_2$ - $P_{21}$ ,  $L_2$ - $P_{22}$ , and  $L_2$ - $P_{23}$ ) and  $PZ_5$  ( $L_4$ - $P_{31}$ ,  $L_4$ - $P_{32}$ ,  $L_4$ - $P_{33}$ ,  $L_5$ - $P_{32}$ ,  $L_5$ - $P_{33}$ , and  $L_5$ - $P_{34}$ ), and observed GWT levels at  $PZ_3$  and  $PZ_5$  as training data. (a) Estimated GWT levels over time at the five drilling and piezometers locations. (b) to (i) Estimated GWT level 2D maps at different dates, with geophone linear array ( $L_{\#}$ ), piezometer ( $PZ_{\#}$ ) and drilling ( $DR_{\#}$ ) positions at the surface. -27-

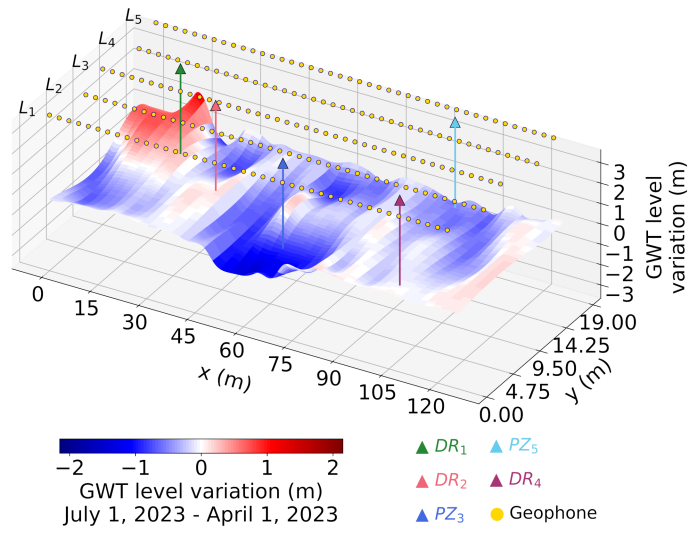


**Figure B3.** Estimated GWT level 2D map variation between high water period (April 1, 2023) and low water period (July 1, 2023), obtained using DCs at seismic array points around  $PZ_3$  ( $L_1$ - $P_{22}$ ,  $L_1$ - $P_{23}$ ,  $L_1$ - $P_{24}$ ,  $L_2$ - $P_{21}$ ,  $L_2$ - $P_{22}$ , and  $L_2$ - $P_{23}$ ) and  $PZ_5$  ( $L_4$ - $P_{31}$ ,  $L_4$ - $P_{32}$ ,  $L_4$ - $P_{33}$ ,  $L_5$ - $P_{32}$ ,  $L_5$ - $P_{33}$ , and  $L_5$ - $P_{34}$ ), and observed GWT levels at  $PZ_3$  and  $PZ_5$  as training data. Geophone, piezometer and drilling positions are displayed at surface.

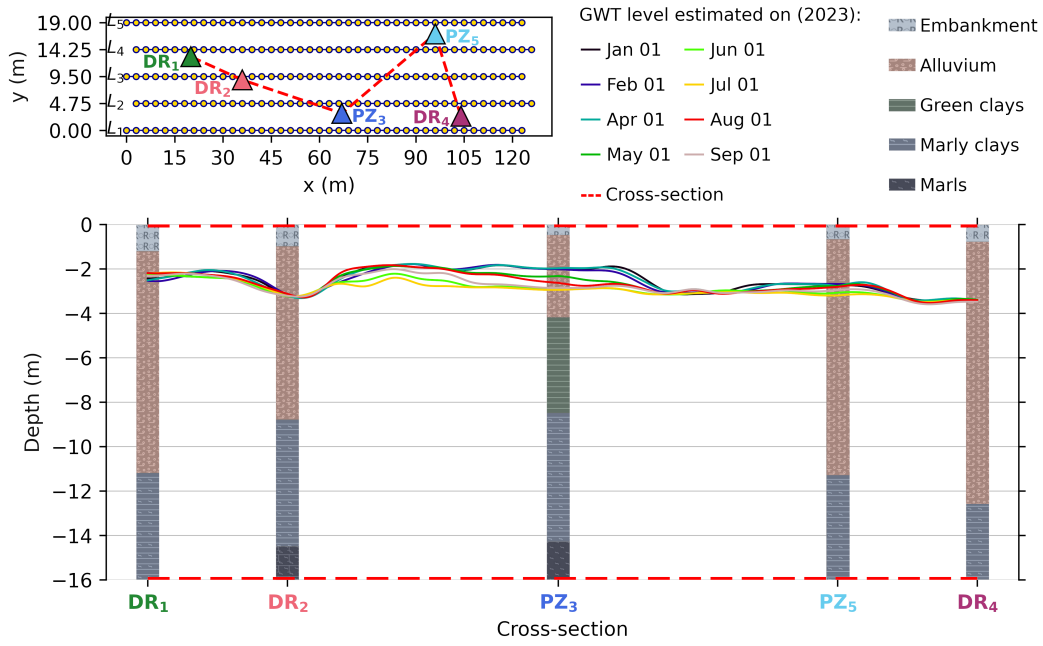


**Figure B4.** (a) Geophone array map and cross-section line (in red) between drilling and piezometers. (b) Cross-section of estimated GWT levels at different dates, obtained using DCs at seismic array points around  $PZ_3$  ( $L_1-P_{22}$ ,  $L_1-P_{23}$ ,  $L_1-P_{24}$ ,  $L_2-P_{21}$ ,  $L_2-P_{22}$ , and  $L_2-P_{23}$ ) and  $PZ_5$  ( $L_4-P_{31}$ ,  $L_4-P_{32}$ ,  $L_4-P_{33}$ ,  $L_5-P_{32}$ ,  $L_5-P_{33}$ , and  $L_5-P_{34}$ ), and observed GWT levels at  $PZ_3$  and  $PZ_5$  as training data, with geologic logs illustrating the nature of the underground materials.

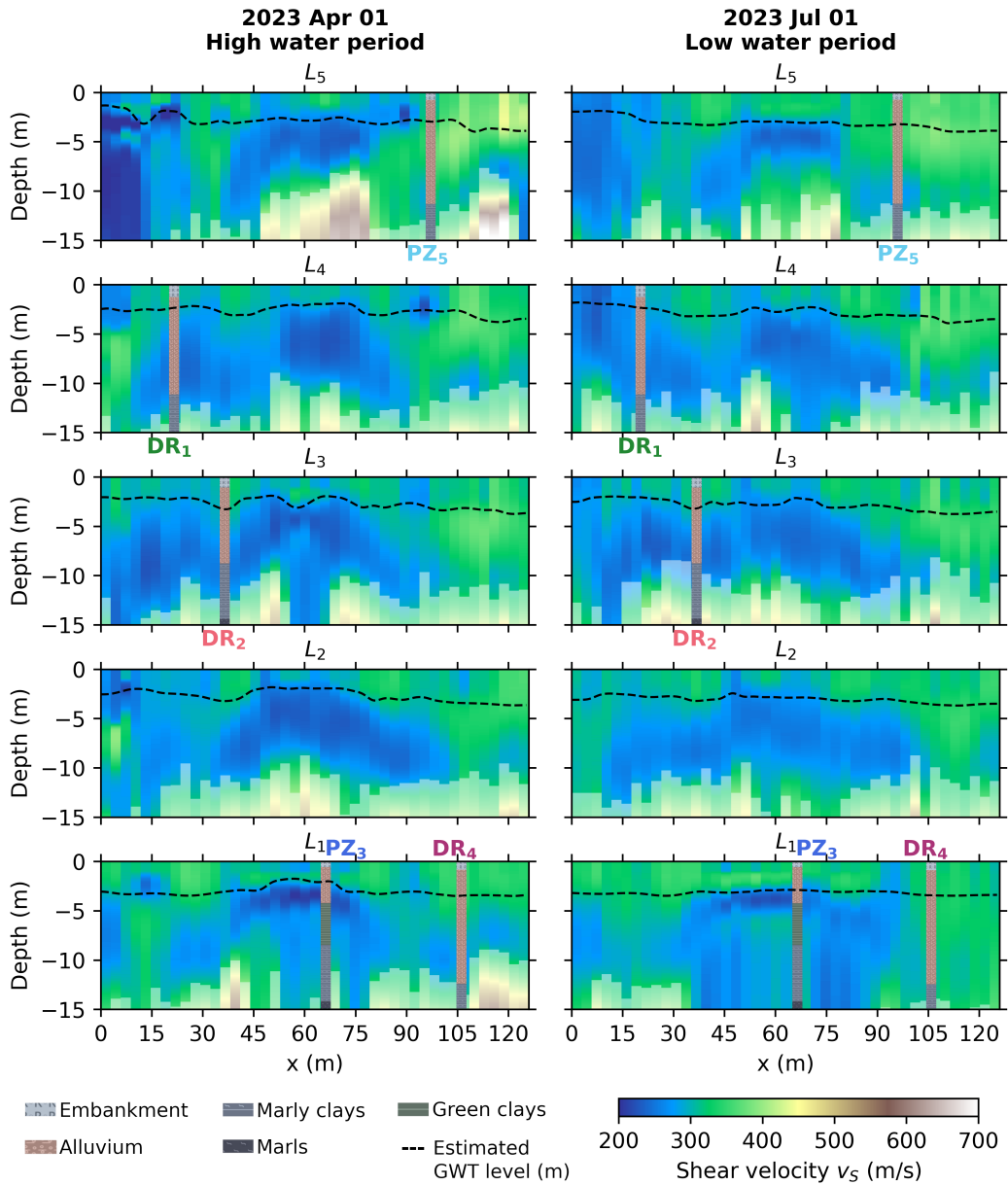


**Figure B5.** Inverted  $V_S$  sections over depth for the 5 linear geophone arrays ( $L_1$  to  $L_5$ ) at a high water period (April 1, 2023) and at a low water period (July 1, 2023). The white mask indicates depths where the standard deviation, between the mean  $V_S$  model and all other accepted models during inversion, is greater than 400 m/s. Estimated GWT levels, obtained using DCs at seismic array points around  $PZ_3$  ( $L_1$ - $P_{22}$ ,  $L_1$ - $P_{23}$ ,  $L_1$ - $P_{24}$ ,  $L_2$ - $P_{21}$ ,  $L_2$ - $P_{22}$ , and  $L_2$ - $P_{23}$ ) and  $PZ_5$  ( $L_4$ - $P_{31}$ ,  $L_4$ - $P_{32}$ ,  $L_4$ - $P_{33}$ ,  $L_5$ - $P_{32}$ ,  $L_5$ - $P_{33}$ , and  $L_5$ - $P_{34}$ ), and observed GWT levels at  $PZ_3$  and  $PZ_5$  as training data., and geologic logs, illustrating the nature of the underground materials at five drilling coordinates, are superposed for interpretation.

## Appendix C Inversion

For each seismic linear array,  $V_R$  over frequencies pseudo-section, corresponding to DCs along  $x$  (fundamental mode  $M_0$ ), obtained by passive-MASW, were inverted to generate a  $V_S$  over depth sections. We use the open-source software package *SWIP*<sup>2</sup> implemented by Pasquet and Bodet (2017), that is built upon the software *Dinver*<sup>3</sup> that uses a *neighbourhood algorithm* developed by (Sambridge, 1999) and implemented by (Wathelet, 2008), to solve the inverse problem in a juxtaposed 1D setup. The inversion was parameterized with five layers, including an half-space, in accordance with the drilling data (see  $PZ_3$  in Figure 1). This method involves a stochastic exploration of a parameter space in order to search for a minimum misfit between measured and simulated DCs. The chosen parameter space, as outlined in Table C1, encompasses various key parameters including layer thicknesses, pressure-wave velocity ( $V_P$ ), shear-wave velocity ( $V_S$ ), density ( $\rho$ ), and Poisson's ratio ( $\nu$ ). The deliberate selection of a large parameter space stems from the limited *a priori* information about the mechanical properties of the geological layers. This approach ensures that the inversion process remains explorative, unbiased, and is capable of capturing a wide range of geological scenarios that may influence the seismic response in the study area. For each DC along the seismic linear arrays, out of a total 200,400 simulated models, only the models with DCs within the error-bars are accepted and averaged to generate final average smooth velocity models. The running parameters using in *SWIP* are outlined in Table C2.

As examples, we present the inversion results at  $PZ_3$  and  $PZ_5$  positions on April 1, 2023, and July 1, 2023. Figure C1 shows the velocity models and corresponding DCs simulated during the inversion on April 1, 2023, and July 1, 2023, respectively. Each DC and velocity model is represented with a color depending on the misfit value (MF) between the experimental data (black crosses and error-bars) and the simulated dispersion defined as:

$$MF = \sqrt{\sum_{i=1}^{N_f} \frac{(V_{sim_i} - V_{exp_i})^2}{N_f \sigma_i^2}}, \quad (C1)$$

<sup>2</sup> <https://github.com/spasquet/SWIP>

<sup>3</sup> [https://www.geopsy.org/wiki/index.php/Dinver:\\_dinverdc](https://www.geopsy.org/wiki/index.php/Dinver:_dinverdc)

442 with  $V_{sim_i}$  and  $V_{exp_i}$  being the simulated and experimental phase velocities at each  
 443 frequency  $f_i$ ,  $N_f$  the number of frequency samples, and  $\sigma_i$  the phase-velocity measurement  
 444 uncertainty (error-bars) at each frequency  $f_i$ .

**Table C1.** Inversion parameter space.

Layer (#)	Thickness (m)	$V_P$ (m/s)	$V_S$ (m/s)	$\rho$ (kg/m <sup>3</sup> )	$\nu$
1	1-10	100-1000	50-500	2000-2500	0.1-0.5
2	1-10	100-1000	50-500	2000-2500	0.1-0.5
3	1-10	100-1000	50-500	2000-2500	0.1-0.5
4	1-20	200-2000	100-1000	2000-2500	0.1-0.5
$\frac{1}{2}$ -space	$\infty$	400-4000	200-2000	2000-2500	0.1-0.5

**Table C2.** Inversion running parameters in *SWIP*.

Parameter	Value	Description
$n_{run}$	4	Number of runs
$it_{max}$	250	Number of iterations per run
$ns_0$	100	Number of starting models
$ns$	200	Number of modes created at each iteration
$nr$	100	Number of previous models to build new sub-parameter space

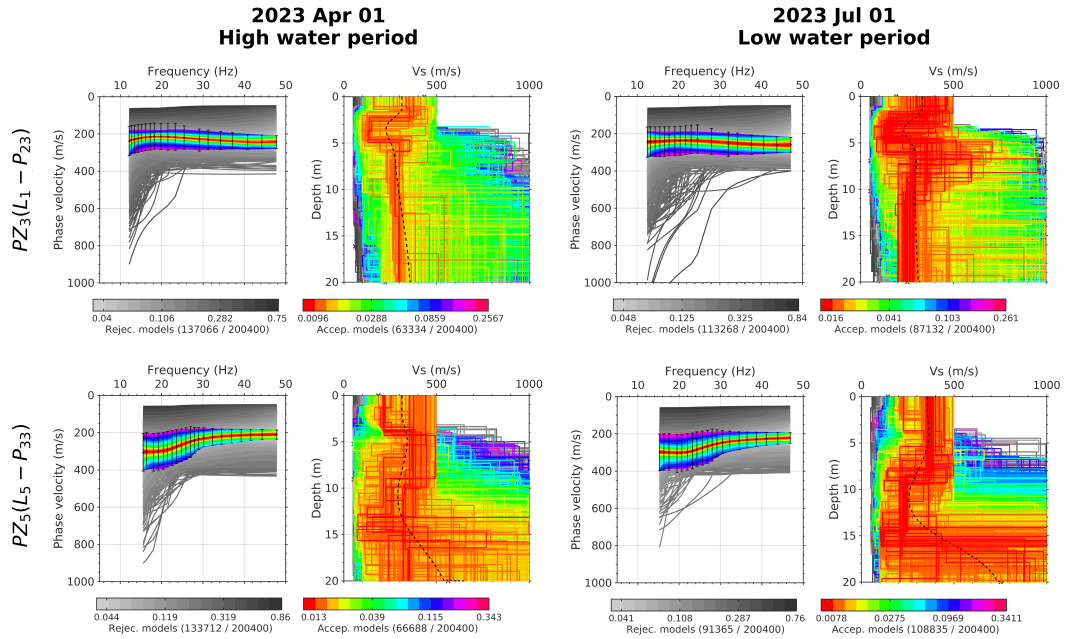


**Figure C1.** Inversion results at seismic array points (top)  $L_1$ - $P_{23}$ , close to  $PZ3$ , and (bottom)  $L_5$ - $P_{33}$ , close to  $PZ5$ , on (left) on April 1, 2023, and July 1, 2023. (a), (c), (e), and (g) show the modeled DCs, with error-bars, for the fundamental mode. (b), (d), (f), and (h) represent the modeled velocity models. Each DC and velocity model is represented with a color depending on the misfit value between the modeled and experimental DCs (black crosses and error-bars). The models inside the error-bars, in terms of DCs, are plotted in color, and the rest are plotted in a gray scale. Plotted from the inversion software *SWIP*.

445 **Appendix D Error computation**

446 The *root mean squared error* (RMSE) corresponds to the expected value of the squared  
 447 error or loss. If  $\hat{y}_i$  is the predicted value of the  $i$ -th samples, and  $y_i$  is the corresponding  
 448 true value, then the RMSE estimated over  $n_{samples}$  is defined as :

$$RMSE(y, \hat{y}) = \frac{1}{n_{samples}} \sum_{i=1}^{n_{samples}} (y_i - \hat{y}_i)^2 . \quad (D1)$$

449 The coefficient of determination, usually denoted  $R^2$ , represents the proportion of  
 450 variance that has been explained by the independent variables in the model. It provides  
 451 an indication of goodness of fit and therefore a measure of how well unseen samples are  
 452 likely to be predicted by the model, through the proportion of explained variance. If  $\hat{y}_i$  is  
 453 the predicted value of the  $i$ -th samples, and  $y_i$  is the corresponding true value, then the  $R^2$   
 454 score over  $n_{samples}$  is defined as :

$$R^2(y, \hat{y}) = 1 - \frac{\sum_{i=1}^{n_{samples}} (y_i - \hat{y}_i)^2}{\sum_{i=1}^{n_{samples}} (y_i - \tilde{y})^2} , \quad (D2)$$

455 where  $\tilde{y} = \frac{1}{n_{samples}} \sum_{i=1}^{n_{samples}} y_i$  is the arithmetic mean value of  $y$ .

## References

- 456
- 457 Abi Nader, A., Albaric, J., Steinmann, M., Hibert, C., Malet, J.-P., Sue, C., ... Boetsch,  
 458 A. (2023). Machine learning prediction of groundwater heights from passive seismic  
 459 wavefield. *Geophysical Journal International*, *234*(3), 1807-1818. doi: 10.1093/gji/  
 460 ggad160
- 461 Aki, K. (1957). Space and time spectra of stationary stochastic waves, with special reference  
 462 to microtremors. *Bulletin of the Earthquake Research Institute*, *35*, 415-456.
- 463 Barajas, A., Poli, P., D'Agostino, N., Margerin, L., & Campillo, M. (2021). Separation of  
 464 poroelastic and elastic processes of an aquifer from tectonic phenomena using geodetic,  
 465 seismic, and meteorological data in the pollino region, italy. *Geochemistry, Geophysics,*  
 466 *Geosystems*, *22*(11), e2021GC009742. doi: 10.1029/2021GC009742
- 467 Bardaine, T., & Rondeleux, B. (2018). *Method and device for monitoring*  
 468 *the subsoil of the earth under a target zone* (patent No. FR3084473B1).  
 469 Retrieved from [https://patents.google.com/patent/WO2020021177A1/  
 470 en?inventor=Bardainne&oq=Bardainne](https://patents.google.com/patent/WO2020021177A1/en?inventor=Bardainne&oq=Bardainne)
- 471 Bardainne, T., Tarnus, R., Deladerriere, N., Hallier, A., Boisson-Gaboriau, J., Valentin, J.,  
 472 ... Bouhdiche, O. (2022). Permanent passive seismic monitoring of the near-surface  
 473 ground beneath railways using trains as sources. In (Vol. 1, p. 14). Fifth International  
 474 Conference on Railway Technology: Research, Development and Maintenance.
- 475 Bardainne, T., Vivin, L., & Tarnus, R. (2023). Railway near-surface passive seismic us-  
 476 ing trains as sources and fiber optic monitoring. In (Vol. 2023, p. 1-5). European  
 477 Association of Geoscientists & Engineers. doi: 10.3997/2214-4609.202320093
- 478 Bergamo, P., Dashwood, B., Uhlemann, S., Swift, R., Chambers, J., Gunn, D., & Donohue,  
 479 S. (2016). Time-lapse monitoring of climate effects on earthworks using surface waves.  
 480 *Geophysics*, *81*, EN1-EN15. doi: 10.1190/GEO2015-0275.1
- 481 Biot, M. A. (1956a). Theory of Propagation of Elastic Waves in a Fluid-Saturated Porous  
 482 Solid. I. Low-Frequency Range. *The Journal of the Acoustical Society of America*,  
 483 *28*(2), 168-178. doi: 10.1121/1.1908239
- 484 Biot, M. A. (1956b). Theory of Propagation of Elastic Waves in a Fluid-Saturated Porous  
 485 Solid. II. Higher Frequency Range. *The Journal of the Acoustical Society of America*,  
 486 *28*(2), 179-191. doi: 10.1121/1.1908241
- 487 Cai, H., Liu, S., Shi, H., Zhou, Z., Jiang, S., & Babovic, V. (2022). Toward improved  
 488 lumped groundwater level predictions at catchment scale: Mutual integration of water

- 489 balance mechanism and deep learning method. *Journal of Hydrology*, *613*, 128495.  
490 doi: <https://doi.org/10.1016/j.jhydrol.2022.128495>
- 491 Cheng, F., Xia, J., Luo, Y., Xu, Z., Wang, L., Shen, C., ... Hu, Y. (2016). Multichan-  
492 nel analysis of passive surface waves based on crosscorrelations. *Geophysics*, *81*(5),  
493 EN57–EN66. doi: 10.1190/geo2015-0505.1
- 494 Cheng, F., Xia, J., Xu, Y., Xu, Z., & Pan, Y. (2015). A new passive seismic method  
495 based on seismic interferometry and multichannel analysis of surface waves. *Journal*  
496 *of Applied Geophysics*, *117*. doi: 10.1016/j.jappgeo.2015.04.005
- 497 Chollet, F., et al. (2015). *Keras*. <https://keras.io>.
- 498 Clements, T., & Denolle, M. A. (2018). Tracking groundwater levels using the ambi-  
499 ent seismic field. *Geophysical Research Letters*, *45*(13), 6459–6465. doi: 10.1029/  
500 2018GL077706
- 501 Cunha Teixeira, J., Bodet, L., Dangeard, M., Gesret, A., Hallier, A., Rivière, A., ... Bois-  
502 son Gaboriau, J. (submitted). Passive measurement of multi-modal surface-wave  
503 dispersion along high-speed lines using uniform linear arrays. *Seismica*.
- 504 Czarny, R., Zhu, T., & Shen, J. (2023). Spatiotemporal evaluation of rayleigh surface wave  
505 estimated from roadside dark fiber das array and traffic noise. *Seismica*, *2*(22). doi:  
506 10.26443/seismica.v2i2.247
- 507 Dafflon, B., Irving, J., & Holliger, K. (2009). Use of high-resolution geophysical data to char-  
508 acterize heterogeneous aquifers: Influence of data integration method on hydrological  
509 predictions. *Water Resources Research*, *45*(9). doi: 10.1029/2008WR007646
- 510 Dagan, G. (1982). Stochastic modeling of groundwater flow by unconditional and conditional  
511 probabilities: 1. conditional simulation and the direct problem. *Water Resources*  
512 *Research*, *18*(4), 813–833. doi: 10.1029/WR018i004p00813
- 513 Dangeard, M., Rivière, A., Bodet, L., Schneider, S., Guérin, R., Jougnot, D., & Mainault,  
514 A. (2021). River corridor model constrained by time-lapse seismic acquisition. *Water*  
515 *Resources Research*, *57*(10), e2020WR028911. doi: 10.1029/2020WR028911
- 516 Derode, A., Larose, E., Tanter, M., de Rosny, J., Tourin, A., Campillo, M., & Fink, M.  
517 (2003). Recovering the green’s function from field-field correlations in an open scatter-  
518 ing medium (1). *The Journal of the Acoustical Society of America*, *113*(6), 2973–2976.  
519 doi: 10.1121/1.1570436
- 520 Foti, S., Hollender, F., Garofalo, F., Albarello, D., Asten, M., Bard, P.-Y., ... Socco,  
521 L. V. (2018). Guidelines for the good practice of surface wave analysis: a product

- 522 of the interpacific project. *Bulletin of Earthquake Engineering*, 16. doi: 10.1007/  
523 s10518-017-0206-7
- 524 Garambois, S., Sénéchal, P., & Perroud, H. (2002). On the use of combined geophysical  
525 methods to assess water content and water conductivity of near-surface formations.  
526 *Journal of Hydrology*, 259, 32-48. doi: 10.1016/s0022-1694(01)00588-1
- 527 Garambois, S., Voisin, C., Romero Guzman, M. A., Brito, D., Guillier, B., & Réfloch, A.  
528 (2019). Analysis of ballistic waves in seismic noise monitoring of water table variations  
529 in a water field site: added value from numerical modelling to data understanding.  
530 *Geophysical Journal International*, 219(3), 1636-1647. doi: 10.1093/gji/ggz391
- 531 Gaubert-Bastide, T., Garambois, S., Bordes, C., Voisin, C., Oxarango, L., Brito, D., &  
532 Roux, P. (2022). High-resolution monitoring of controlled water table variations from  
533 dense seismic-noise acquisitions. *Water Resources Research*, 58(8), e2021WR030680.  
534 doi: 10.1029/2021WR030680
- 535 Grêt, A., Snieder, R., & Scales, J. (2006). Time-lapse monitoring of rock properties with  
536 coda wave interferometry. *Journal of Geophysical Research: Solid Earth*, 111(B3).  
537 doi: 10.1029/2004JB003354
- 538 Gutiérrez, F., Parise, M., De Waele, J., & Jourde, H. (2014). A review on natural and  
539 human-induced geohazards and impacts in karst. *Earth-Science Reviews*, 138, 61–88.  
540 doi: 10.1016/j.earscirev.2014.08.002
- 541 Hermans, T., Goderniaux, P., Jougnot, D., Fleckenstein, J. H., Brunner, P., Nguyen, F.,  
542 ... Le Borgne, T. (2023). Advancing measurements and representations of subsurface  
543 heterogeneity and dynamic processes: towards 4d hydrogeology. *Hydrology and Earth  
544 System Sciences*, 27(1), 255–287. doi: 10.5194/hess-27-255-2023
- 545 Jougnot, D., Linde, N., Haarder, E., & Looms, M. (2015). Monitoring of saline tracer  
546 movement with vertically distributed self-potential measurements at the hobe agri-  
547 cultural site, voulund, denmark. *Journal of Hydrology*, 521, 314-327. doi: 10.1016/  
548 j.jhydrol.2014.11.041
- 549 Kim, D., & Lekic, V. (2019). Groundwater variations from autocorrelation and re-  
550 ceiver functions. *Geophysical Research Letters*, 46(23), 13722-13729. doi: 10.1029/  
551 2019GL084719
- 552 Kingma, D., & Ba, J. (2014). Adam: A method for stochastic optimization. *International  
553 Conference on Learning Representations*.
- 554 Kleinhans, M. G. (2005). Flow discharge and sediment transport models for estimating a

- 555 minimum timescale of hydrological activity and channel and delta formation on mars.  
556 *Journal of Geophysical Research: Planets*, 110(E12). doi: 10.1029/2005JE002521
- 557 Klotzsche, A., Jonard, F., Looms, M., van der Kruk, J., & Huisman, J. (2018). Measuring  
558 soil water content with ground penetrating radar: A decade of progress. *Vadose Zone*  
559 *Journal*, 17(1), 180052. doi: 10.2136/vzj2018.03.0052
- 560 Larose, E., Carrière, S., Voisin, C., Bottelin, P., Baillet, L., Guéguen, P., ... Massey, C.  
561 (2015). Environmental seismology: What can we learn on earth surface processes  
562 with ambient noise? *Journal of Applied Geophysics*, 116, 62–74. doi: 10.1016/  
563 j.jappgeo.2015.02.001
- 564 Lecocq, T., Longuevergne, L., Pedersen, H., Brenguier, F., & Stammer, K. (2017). Moni-  
565 toring ground water storage at mesoscale using seismic noise: 30 years of continuous  
566 observation and thermo-elastic and hydrological modeling. *Scientific Reports*, 7. doi:  
567 10.1038/s41598-017-14468-9
- 568 Linnainmaa, S. (1976). Taylor expansion of the accumulated rounding error. *BIT Numerical*  
569 *Mathematics*, 16(2), 146–160. doi: 10.1007/BF01931367
- 570 Loeffler, O. H., & Bano, M. (2004). Ground penetrating radar measurements in a controlled  
571 vadose zone: influence of the water content. *Vadose Zone Journal*, 3, 1082-1092. doi:  
572 10.2113/3.4.1082
- 573 Lu, Z. (2014). Feasibility of using a seismic surface wave method to study seasonal and  
574 weather effects on shallow surface soils. *Journal of Environmental & Engineering*  
575 *Geophysics*, 19, 71-85. doi: 10.2113/JEEG19.2.71
- 576 Maillot, M., Flipo, N., Rivière, A., Desassis, N., Renard, D., Goblet, P., & Vincent, M.  
577 (2019). Technical note: Water table mapping accounting for river–aquifer connectivity  
578 and human pressure. *Hydrology and Earth System Sciences*, 23(11), 4835–4849. doi:  
579 10.5194/hess-23-4835-2019
- 580 Mao, S., Lecointre, A., van der Hilst, R., & Campillo, M. (2022). Space-time monitoring  
581 of groundwater fluctuations with passive seismic interferometry. *Nature Communica-*  
582 *tions*, 13, 4643. doi: 10.1038/s41467-022-32194-3
- 583 Mi, B., Xia, J., Tian, G., Shi, Z., Xing, H., Chang, X., ... Zhang, H. (2022). Near-surface  
584 imaging from traffic-induced surface waves with dense linear arrays: An application  
585 in the urban area of hangzhou, china. *Geophysics*, 87(2), B145–B158. doi: 10.1190/  
586 geo2021-0184.1
- 587 Mi, B., Xia, J., Xu, Y., You, B., & Chen, Y. (2023). Retrieval of surface waves from

- 588 high-speed-train-induced vibrations using seismic interferometry. *Geophysics*. doi:  
589 10.1190/geo2022-0603.1
- 590 Murtagh, F. (1991). Multilayer perceptrons for classification and regression. *Neurocomput-*  
591 *ing*, 2(5), 183-197. doi: 10.1016/0925-2312(91)90023-5
- 592 Nguyen-Thé, D., Ollagnier, S., Pétrignet, M., Thonnon, J., & Joannes, O. (2010). *Carte*  
593 *piézométrique de la nappe des grès du Trias inférieur de 2010. Report BRGM/RP-*  
594 *59294-FR.*
- 595 Panda, S., Kumar, S., Pradhan, S., Sidhu, J., Kralia, A., & Thakur, D. M. (2022). Effect  
596 of groundwater table fluctuation on slope instability: a comprehensive 3d simulation  
597 approach for kotropi landslide, india. *Landslides*. doi: 10.1007/s10346-022-01993-6
- 598 Parise, M. (2019). Sinkholes. In W. B. White, D. C. Culver, & T. Pipan (Eds.), *Encyclopedia*  
599 *of caves (third edition)* (Third ed., p. 934-942). Academic Press. doi: 10.1016/B978-0  
600 -12-814124-3.00110-2
- 601 Park, C. B., & Miller, R. D. (2008). Roadside Passive Multichannel Analysis of Surface  
602 Waves (MASW). *Journal of Environmental and Engineering Geophysics*, 13(1), 1–11.  
603 doi: 10.2113/JEEG13.1.1
- 604 Park, C. B., Miller, R. D., & Xia, J. (1999). Multichannel analysis of surface waves.  
605 *Geophysics*, 64(3), 800–808. doi: 10.1190/1.1444590
- 606 Pasquet, S., & Bodet, L. (2017). Swip: An integrated workflow for surface-wave dispersion  
607 inversion and profiling. *Geophysics*, 82(6), WB47–WB61. doi: 10.1190/geo2016-0625  
608 .1
- 609 Pasquet, S., Bodet, L., Dhemaied, A., Mouhri, A., Vitale, Q., Rejiba, F., ... Guérin, R.  
610 (2015a). Detecting different water table levels in a shallow aquifer with combined  
611 p-, surface and sh-wave surveys: Insights from vp/vs or poisson's ratios. *Journal of*  
612 *Applied Geophysics*, 113. doi: 10.1016/j.jappgeo.2014.12.005
- 613 Pasquet, S., Bodet, L., Longuevergne, L., Dhemaied, A., Camerlynck, C., Rejiba, F., &  
614 Guérin, R. (2015b). 2d characterization of near-surface vp/vs: Surface-wave dispersion  
615 inversion versus refraction tomography. *Near Surface Geophysics*, 13. doi: 10.3997/  
616 1873-0604.2015028
- 617 Qin, L., Steidl, J. H., Qiu, H., Nakata, N., & Ben-Zion, Y. (2022). Monitoring seasonal  
618 shear wave velocity changes in the top 6 m at garner valley in southern california with  
619 borehole data. *Geophysical Research Letters*, 49(23), e2022GL101189. doi: 10.1029/  
620 2022GL101189

- 621 Quiros, D. A., Brown, L. D., & Kim, D. (2016). Seismic interferometry of railroad induced  
622 ground motions: body and surface wave imaging. *Geophysical Journal International*,  
623 *205*(1), 301-313. doi: 10.1093/gji/ggw033
- 624 Rahardjo, H., Satyanaga, A., Leong, E., & Ng, Y. (2010). Effects of groundwater table  
625 position and soil properties on stability of slope during rainfall. *Journal of Geotechnical*  
626 *and Geoenvironmental Engineering*, *136*, 1555–1564. doi: 10.1061/(ASCE)GT.1943  
627 -5606.0000385
- 628 Rezaeifar, M., Lavoué, F., Maggio, G., Xu, Y., Bean, C. J., Pinzon-Rincon, L., ... Bren-  
629 guier, F. (2023). Imaging shallow structures using interferometry of seismic body  
630 waves generated by train traffic. *Geophysical Journal International*, *233*(2), 964–977.  
631 doi: 10.1093/gji/ggac507
- 632 Rosenblatt, F. (1958). The perceptron: A probabilistic model for information storage  
633 and organization in the brain. *Psychological Review*, *65*(6), 386–408. doi: 10.1037/  
634 h0042519
- 635 Sambridge, M. (1999). Geophysical inversion with a neighbourhood algorithm—i. searching  
636 a parameter space. *Geophysical Journal International*, *138*(2), 479–494. doi: 10.1046/  
637 j.1365-246X.1999.00876.x
- 638 Samouëlian, A., Cousin, I., Tabbagh, A., Bruand, A., & Richard, G. (2005). Electrical  
639 resistivity survey in soil science: a review. *Soil and Tillage Research*, *83*(2), 173-193.  
640 doi: 10.1016/j.still.2004.10.004
- 641 Sanchez Gonzalez, R., Bodet, L., Gesret, A., & Rivière, A. (in prep). Bayesian estimation  
642 of van Genuchten parameters in unsaturated and unconsolidated soils using seismic  
643 data. *Geophysical Journal International*.
- 644 Shorten, C., & Khoshgoftaar, T. M. (2019). A survey on image data augmentation for deep  
645 learning. *Journal of Big Data*, *6*(1), 60. doi: 10.1186/s40537-019-0197-0
- 646 Shtivelman, V. (1999). Using surface waves for estimating shear wave velocities in the  
647 shallow subsurface onshore and offshore israel. *European Journal of Environmental*  
648 *and Engineering Geophysics*, *4*, 15-35.
- 649 Solazzi, S. G., Bodet, L., Holliger, K., & Jougnot, D. (2021). Surface-wave dispersion in  
650 partially saturated soils: The role of capillary forces. *Journal of Geophysical Research:*  
651 *Solid Earth*, *126*(12), e2021JB022074. doi: 10.1029/2021JB022074
- 652 Tarnus, R., Bardainne, T., Michel, L., Deladerriere, N., & Cai, C. (2022a). A case study for  
653 railway underground imaging using trains as seismic signal for sinkhole and subsidence

- 654 phenomena prevention. In (Vol. 1, p. 13). Fifth International Conference on Railway  
655 Technology: Research, Development and Maintenance.
- 656 Tarnus, R., Bardainne, T., Michel, L., Deladerriere, N., Cai, C., Hallier, A., & Boisson-  
657 Gaboriau, J. (2022b). A case study for underground imaging using trains as seismic  
658 signal to investigate subsidence phenomena. In (Vol. 2022, p. 1-5). European Associ-  
659 ation of Geoscientists & Engineers. doi: 10.3997/2214-4609.202220033
- 660 Tripathy, K., & Mishra, A. (2024). Deep learning in hydrology and water resources disci-  
661 plines: Concepts, methods, applications, and research directions. *Journal of Hydrol-*  
662 *ogy*, 628, 130458. doi: 10.1016/j.jhydrol.2023.130458
- 663 Tsai, F. T.-C., & Li, X. (2008). Inverse groundwater modeling for hydraulic conductivity  
664 estimation using bayesian model averaging and variance window. *Water Resources*  
665 *Research*, 44(9). doi: 10.1029/2007WR006576
- 666 Voisin, C., Garambois, S., Massey, C., & Brossier, R. (2016). Seismic noise monitoring of the  
667 water table in a deep-seated, slow-moving landslide. *Interpretation*, 4(3), SJ67-SJ76.  
668 doi: 10.1190/INT-2016-0010.1
- 669 Voisin, C., Guzmán, M., Réfloch, A., Taruselli, M., & Garambois, S. (2017). Groundwa-  
670 ter monitoring with passive seismic interferometry. *Journal of Water Resource and*  
671 *Protection*, 9, 1414-1427. doi: 0.4236/jwarp.2017.912091
- 672 Waltham, T., Bell, F., & Culshaw, M. (2004). *Sinkholes and subsidence: karst and cavernous*  
673 *rocks in engineering and construction* (2005th ed.). Springer. doi: 10.1007/b138363
- 674 Wapenaar, K. (2004). Retrieving the elastodynamic green's function of an arbitrary in-  
675 homogeneous medium by cross correlation. *Physical Review Letters*, 93(25), 254301.  
676 doi: 10.1103/PhysRevLett.93.254301
- 677 Wapenaar, K., Draganov, D., Snieder, R., Campman, X., & Verdel, A. (2010a). Tutorial  
678 on seismic interferometry. part i: Basic principles and applications. *Geophysics*, 75,  
679 75A195-75209. doi: 10.1190/1.3457445
- 680 Wapenaar, K., Slob, E., Snieder, R., & Curtis, A. (2010b). Tutorial on seismic interferom-  
681 etry: Part 2 — underlying theory and new advances. *Geophysics*, 75, 75A211-75227.  
682 doi: 10.1190/1.3463440
- 683 Wathelet, M. (2008). An improved neighborhood algorithm: Parameter conditions and  
684 dynamic scaling. *Geophysical Research Letters*, 35(9). doi: 10.1029/2008GL033256
- 685 Weaver, R. L., & Lobkis, O. I. (2004). Diffuse fields in open systems and the emergence  
686 of the green's function (1). *The Journal of the Acoustical Society of America*, 116(5),

- 687 2731–2734. doi: 10.1121/1.1810232
- 688 Werbos, P. J. (1982). Applications of advances in nonlinear sensitivity analysis. In  
689 R. F. Drenick & F. Kozin (Eds.), *System modeling and optimization* (pp. 762–770).  
690 Berlin, Heidelberg: Springer Berlin Heidelberg.
- 691 Xiao, X., Gutiérrez, F., & Guerrero, J. (2020). The impact of groundwater drawdown and  
692 vacuum pressure on sinkhole development. physical laboratory models. *Engineering  
693 Geology*, 279, 105894. doi: 10.1016/j.enggeo.2020.105894
- 694 Ying, X. (2019). An overview of overfitting and its solutions. *Journal of Physics: Conference  
695 Series*, 1168, 022022. doi: 10.1088/1742-6596/1168/2/022022
- 696 You, B., Mi, B., Guan, B., Zhang, H., & Liu, Y. (2023). High-quality surface wave retrieval  
697 from vibrations generated by high-speed trains moving on viaducts. *Journal of Applied  
698 Geophysics*, 212, 105005. doi: 10.1016/j.jappgeo.2023.105005
- 699 Zhang, S., Luo, B., Ben-Zion, Y., Lumley, D. E., & Zhu, H. (2023). Monitoring ter-  
700 restrial water storage, drought and seasonal changes in central oklahoma with am-  
701 bient seismic noise. *Geophysical Research Letters*, 50(17), e2023GL103419. doi:  
702 10.1029/2023GL103419